Heliyon 10 (2024) e38780

Contents lists available at ScienceDirect

Heliyon

journal homepage: www.cell.com/heliyon

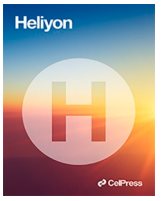

Research article

# Fabrication of a novel magnetic carbon nanotube coated with polydopamine modified with EDTA for removing $Cd^{2+}$ and $Pb^{2+}$ ions from an aqueous solution

Marzie Esmaeili Chermahini [a], Mehran Ghiaci [a,*], Alireza Najafi Chermahini [a], Mehran Shirvani [b]

[a] Department of Chemistry, Isfahan University of Technology, Isfahan, 8415683111, Iran
[b] Department of Agriculture, Isfahan University of Technology, Isfahan, 8415683111, Iran

ARTICLE INFO

*Keywords:*
Polydopamine
Carbon nanotubes
EDTA dianhydride
Magnetic adsorbent
Heavy metal ions

ABSTRACT

This work demonstrates the preparation of a new, effective, and reusable magnetic adsorbent by functionalizing dopamine with ethylenediaminetetraacetic dianhydride and polymerizing it on the surface of magnetic carbon nanotubes (EDTA@PD-CNT/$Fe_3O_4$). The adsorbent was analyzed using XRD, FT-IR, Zeta potential, FE-SEM, EDX, BET, TGA, DTA, and VSM. The synthesized adsorbent was used to remove lead and cadmium ions from aqueous solution. The adsorption process was improved by optimizing key parameters such as pH, adsorbent dosage, contact time, and ion concentration. For both ions, the thermodynamic data of the processes and adsorption kinetics were examined. Analyzing the experimental data revealed that the Langmuir isotherm was the most appropriate model, and the examination of adsorption kinetics showed a pseudo-second-order equation. The adsorption process by the EDTA@PD-CNT/$Fe_3O_4$ adsorbent was spontaneous and endothermic, according to the thermodynamic data, for $Cd^{2+}$ and $Pb^{2+}$, the highest adsorption capacities were found to be 204.54 mg $g^{-1}$ and 376.48 mg $g^{-1}$, respectively.

## 1. Introduction

The rapid expansion and advancement of the global economy have led to heightened concern regarding the introduction of heavy metal contaminants into the environment through industrial activities such as battery manufacturing, metallurgy, smelting, and energy production [1–3]. Unlike other contaminants, these chemicals are non-biodegradable and can bioaccumulate in biological tissues [4,5]. Cadmium ($Cd^{2+}$) and lead ($Pb^{2+}$) are non-biodegradable metals that have attracted a lot of attention due to their potential to cause anemia, mental retardation, cancer, kidney and liver disorder, and lung inflammation [6,7]. Hence, the removal of this specific group of environmental contaminants is crucial for the enhancement and purification of the environment [8,9].

Extraction [10], chemical precipitation [11], oxidation [12], ion exchange [13], electrochemistry [14], and nanofiltration [15] are among the techniques that have been used to remove $Cd^{2+}$ and $Pb^{2+}$ ions from the water environment. However, the lack of popularity of these techniques can be attributed to their difficult recovery, complex processes, and high cost [16,17]. Adsorption is considered a highly promising method for removal applications because of its simple operation, economic advantages, easy recovery, and potential for reuse [18,19].

* Corresponding author.
*E-mail address:* mghiaci@iut.ac.ir (M. Ghiaci).

https://doi.org/10.1016/j.heliyon.2024.e38780
Received 16 April 2024; Received in revised form 25 September 2024; Accepted 30 September 2024
Available online 2 October 2024

Metal oxides [20], biosorbents [21], resins [22], coal [23], and carbon nanomaterials [24] are among the materials that show surface adsorption [25]. Carbon nanostructures, such as carbon nanotubes, were considered appropriate substrates for adsorption because of their exceptional mechanical and electrical characteristics, extensive surface area, and chemical stability [26,27]. Considering the limited adsorption capacity, slow separation, and low reusability of adsorbents, surface modification of carbon nanotubes to create more efficient adsorbents in the field of heavy metal removal has been given priority [28,29].

Ethylenediaminetetraacetic acid (EDTA) as a substrate modifier can increase the adsorption capacity due to its chelating structure (including carboxyl groups and amine groups) and its ability to coordinate with a wide range of metal ions [30–32]. Several materials, such as metal-organic frameworks (MOFs) [33], chitosan [34], graphene oxide [35], polymers [36], functionalized $Fe_3O_4$ [37], modified cellulose [38], and biomass [39] were modified with EDTA to improve their capacity to adsorb heavy metals [40]. The efficacy of adsorbents containing EDTA is contingent upon the characteristics of the substrate and the substance responsible for binding EDTA to the substrate [31,35]. To transfer the coordination properties of EDTA to the substrate, one can employ ethylenediaminetetraacetic dianhydride (EDTAD) as a derivative of this molecule. Utilizing dopamine for the amination reaction with EDTAD, followed by polymerization on the substrate's surface, can serve as an effective technique for linking ETDA to the substrate. Meanwhile, the procedure of separating the adsorbent from the aqueous environment has significance for minimizing waste and saving time [41]. The fabrication of magnetic nanoparticles, such as $Fe_3O_4$, on the substrate's surface allows for efficient and rapid separation of the adsorbent using an external magnetic field [42,43]. Most of the reported hosts of EDTA functionalized adsorbents have used a bulk framework like chitosan, cellulose, MOF, etc., and one could not expect to functionalize the framework with a maximum amount of EDTAD because of the bulky structure of the molecule. In this respect, we thought that to increase the capacity of the adsorbent, it is better to functionalize the monomer and then polymerize it on a surface with an efficient surface area. Therefore, the objective of this work was to establish an innovative sorbent based on dopamine for the removal of heavy metal ions such as cadmium and lead. It was clear that by functionalizing the dopamine, it would lose some of its toughness. However, as we will discuss in the coming sections, the prepared adsorbent, i.e., EDTA@PD-CNT/$Fe_3O_4$, achieved one of the highest adsorption capacities of 376.48 and 204.54 mg $g^{-1}$ for $Pb^{2+}$ and $Cd^{2+}$, respectively. The characteristics of this adsorbent can be mentioned as easy separation, ease of recovery, and reusability. The structure and properties of the synthesized composite have been evaluated and determined using XRD, FT-IR, EDX, FE-SEM, Zeta potential, BET, VSM, TGA, and DTA analysis. The effect of adsorbent dose, temperature, pH, reaction time, concentration, and the adsorption of both ions was investigated separately. Adsorption kinetics and isotherms, as well as thermodynamic parameters, and finally, the maximum adsorption capacity of the sorbent, were measured.

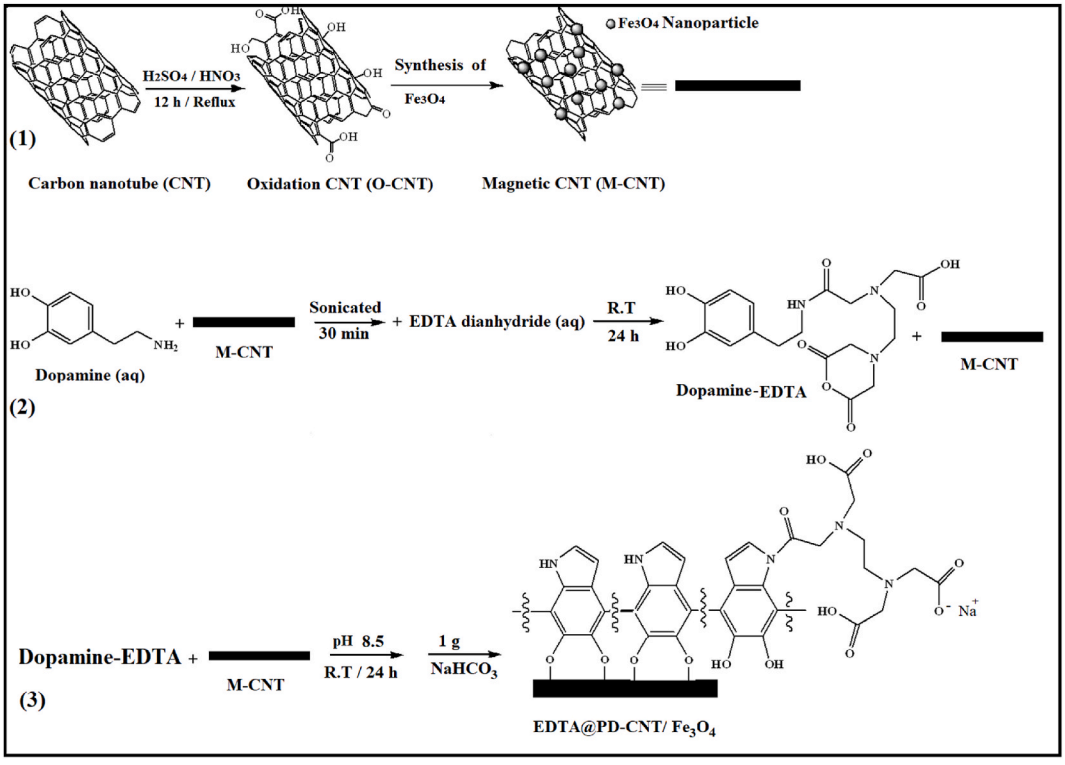


**Fig. 1.** Schematic synthesis of magnetic adsorbent (EDTA@PD-CNT/$Fe_3O_4$).

## 2. Experiments and methods

### 2.1. Materials

All the chemicals have been utilized at high purity levels without pretreatment and are readily available. The materials used to prepare the magnetic adsorbent were MWCNT, ethylenediaminetetraacetic dianhydride (EDTAD) (98 % Sigma-Aldrich), dopamine hydrochloride (Sigma-Aldrich), $FeCl_3.6H_2O$, $FeCl_2.4H_2O$, $HNO_3$, $H_2SO_4$, ammonia solution (25 %), sodium acetate, ethylene glycol, ethanol, tris-base and deionized water. Standard solutions were prepared by employing salts of $Pb(NO_3)_2$ and $Cd(NO_3)_2.4H_2O$, which contain heavy metal ions. Solutions of HCl and NaOH with a concentration of 0.01 M were employed to control the pH.

### 2.2. Preparation of adsorbent

Fig. 1 illustrates the overall process for designing the EDTA@PD-CNT/$Fe_3O_4$ composite.

#### 2.2.1. Synthesis of M-CNT

The initial step involved the oxidation of the carbon nanotube surface using $HNO_3$ and $H_2SO_4$, followed by the synthesis of $Fe_3O_4$ nanoparticles on the surface of the CNTs. The oxidized carbon nanotubes (O-CNTs) were prepared based on a procedure reported in the literature [44]. 0.5 g of multi-walled carbon nanotubes (CNTs) were added to 50 mL of a solution containing 25 mL of $HNO_3$ (6N) and 25 mL of $H_2SO_4$ (2N), and the mixture was refluxed for 12 h. The O-CNTs were separated by centrifugation and washed by deionized water until the solution was entirely neutral. The solid was finally vacuum-dried at 50 °C. Magnetic carbon nanotubes (M-CNTs) were synthesized using the following method: At first, 0.20 g of O-CNT was added to 70 mL of ethylene glycol and sonicated for 15 min. In the next step, 1.014 g of $FeCl_3.6H_2O$ and 0.414 g of $FeCl_2.4H_2O$ were added and sonicated again for 15 min. After adding 2.16 g of sodium acetate, the mixture was sonicated again for 15 min. Finally, 20 mL of ammonia solution (25 %) was added, and the mixture was stirred for 30 min. The suspension was transferred to a Teflon-lined autoclave and treated at 180 °C for 6 h. The M-CNT precipitate was separated by the magnet and washed several times with ethanol and deionized water. The magnetic carbon nanotubes were dried in a vacuum oven at 60 °C for 12 h [45].

#### 2.2.2. Synthesis of M-CNT/Dopamine-EDTA

During the second step, 0.30 g of the M-CNT and 0.60 g of dopamine hydrochloride were suspended in 50 mL of deionized water and sonicated for 30 min 1.20 g of EDTAD dissolved in 20 mL of deionized water was added to the mixture, and the resulting mixture was sonicated for 30 min and then stirred overnight at room temperature. Dopamine reacts with the anhydride ring in the EDTAD molecule and causes the ring to open [46,47].

#### 2.2.3. Synthesis of EDTA@PD-CNT/$Fe_3O_4$

Polydopamine was synthesized on the surface of M-CNT by changing the pH to 8.5 in the third step [48]. The mixture was agitated for 24 h at ambient temperature using a magnetic stirrer. After the dopamine polymerization was completed, to ensure the complete hydrolysis of EDTAD, 1 g of $NaHCO_3$ was added to the above solution, and the solution was stirred for 1 h [28]. Subsequently, the resulting solid was rinsed many times with deionized water and isolated using an external magnetic field. The final composite was dehydrated in a vacuum oven at 60 °C.

### 2.3. Characterization of the samples

The surface morphology and energy dispersive spectroscopy (EDS) measurements of all samples (CNT, O-CNT, M-CNT, and EDTA@PD-CNT/$Fe_3O_4$) were analyzed using a field emission scanning electron microscope (FE-SEM/QUANT, model FEG-450, FEI, USA). A BET (BELSORP miniII, Japan) analysis was used to find out the specific surface area and the porosity of the samples. A simultaneous thermal analysis (STA/PerkinElmer STA6000, USA) was used to see how the samples responded to changes in temperature. The graphs related to differential thermal analysis (DTA) and thermal analysis (TGA) were obtained for all samples. To ascertain the synthesis of the ultimate adsorbent and discern the functional groups included in the samples at each stage, the FT-IR spectrum (model Tensor 27, Bruker, Germany) of all the samples was investigated in the range of 400–4000 $cm^{-1}$. The crystallinity and phase of the CNT, M-CNT, and EDTA@PD-CNT/$Fe_3O_4$ samples were determined by X-ray diffraction analysis (XRD/ASENWARE/AW-XDM300). Finally, a vibrating sample magnetometer (VSM/MDK, Iran) was used to find the hysteresis loops of the EDTA@PD-

**Table 1**
Specific surface area and morphological characterization of the samples using BET and BJH equation.

| Sample | BET | | | |
|---|---|---|---|---|
| | S ($m^2.g^{-1}$) | $V_m$ ($cm^3.g^{-1}$) | Total pore volume ($cm^3.g^{-1}$) | Mean pore diameter (nm) |
| CNT | 146.49 | 33.66 | 0.34 | 9.34 |
| O-CNT | 170.97 | 39.28 | 0.38 | 9.00 |
| M-CNT | 122.64 | 28.18 | 0.22 | 11.17 |
| EDTA@PD-CNT/$Fe_3O_4$ | 46.12 | 10.60 | 0.09 | 9.42 |

CNT/$Fe_3O_4$ adsorbent. In addition, DLS-ZETA (model SZ-100/HORIBA/Japan) was used to measure the surface charge of the adsorbent at various pH levels.

### 2.4. Adsorption experiments

The effectiveness of the magnetic EDTA@PD-CNT/$Fe_3O_4$ adsorbent in removing $Cd^{2+}$ and $Pb^{2+}$ from the water was evaluated by batch adsorption test. Nitrate salts were used as sources of $Cd^{2+}$ and $Pb^{2+}$ ions. Every test was carried out in a 100 mL polypropylene (PP) container. After the adsorption trials, the adsorbent was first separated from the aqueous solution using an external magnetic field. Subsequently, the remaining concentration of metal ions was analyzed using an atomic adsorption spectrophotometer (AAS/RAYLEIGH, WFX-210). The adsorption equations presented in Table 7 (Eqs. 1(a), 1(b), and 1(c)) were utilized to determine the equilibrium adsorption capacity ($Q_e$), adsorption capacity at time t ($Q_t$), and removal efficiency (%R) of the adsorbent. Solutions with varying pH values (ranging from 2 to 7) that contained 50 ppm of $Cd^{2+}$ or $Pb^{2+}$ ions were made to assess the impact of pH on the adsorption process. 20 mL of the prepared solutions were mixed with 5 mg of adsorbent. To monitor the adsorbent dosage test, different amounts of adsorbent (3–15 mg) were mixed with 20 mL of 50 ppm (pH = 6) $Cd^{2+}$ or $Pb^{2+}$ solutions. The samples were shaken for an hour at 200 rpm and at 25 °C.

### 2.5. Adsorption kinetic

An amount of 5 mg of adsorbent was introduced into the solutions containing $Pb^{2+}$, whereas 8 mg was added to the solutions containing $Cd^{2+}$ to conduct time factor experiments. The adsorption reaction was conducted at 25 °C with a speed of 200 rpm at different times (0–360 min). The experimental data were analyzed using the pseudo-first-order (Eq. (2), Table 7), pseudo-second-order (Eq. (3), Table 7), and Elovich (Eq. (4), Table 7) kinetic models. The intra-particle diffusion (IPD) kinetics model (Eq. (5), Table 7) was employed to ascertain the rate-limiting step and precise mechanism of adsorption.

### 2.6. Adsorption isotherm studies

In the optimal conditions, the concentration factor test was done by adding the adsorbent to 20 mL of solutions with varying amounts (10–200 ppm) of $Cd^{2+}$ or $Pb^{2+}$ ions. Employed the Langmuir and Freundlich isotherm models to simulate experimental data. The non-linear relationships of Langmuir and Freundlich isotherms are expressed by Eqs. (6) and (7) in Table 7, respectively. Eq. (6) in Table 7 allows us to determine the maximum adsorption capacity for $Cd^{2+}$ or $Pb^{2+}$ ions.

### 2.7. Adsorption thermodynamic

To examine the impact of temperature on the adsorption process and obtain thermodynamic parameters, concentration factor tests were carried out at three different temperatures (298, 303, and 308 K). Equations (9) and (10) in Table 7 present thermodynamic relations along with parameters.

### 2.8. Evaluating the efficiency of the adsorbent in the binary adsorption system

The experiment completed for each ion was analyzed separately, followed by research on the adsorbent's behavior in the binary adsorption system. Solutions were created that consisted of a combination of $Cd^{2+}$ and $Pb^{2+}$ ions. The pH of all solutions was set to 6.

**Table 2**
Kinetic parameters for adsorption of $Pb^{+2}$ and $Cd^{+2}$ by EDTA@PD-CNT/$Fe_3O_4$ using non-linear fitting.

| Adsorption kinetic | Parameter | Value | |
|---|---|---|---|
| | | $Pb^{+2}$ | $Cd^{+2}$ |
| PFO | $k_1$ ($min^{-1}$) | 0.070 | 0.068 |
| | Qe.cal. ($mg.g^{-1}$) | 187.5 | 117.8 |
| | $R^2$ | 0.937 | 0.935 |
| PSO | $k_2 \times 10^{-4}$ ($mg^{-1}.min^{-1}.g$) | 6 | 9.29 |
| | Qe.cal. ($mg.g^{-1}$) | 199 | 125 |
| | $R^2$ | 0.982 | 0.982 |
| Elovich | α | 256 | 148 |
| | β | 0.039 | 0.061 |
| | $R^2$ | 0.973 | 0.975 |
| IPD | $k_{i1}$ | 14.81 | 9.25 |
| | $R_{i1}^2$ | 0.991 | 0.991 |
| | $k_{i2}$ | 0.36 | 0.34 |
| | $R_{i2}^2$ | 0.985 | 0.995 |

**Table 3**
The parameters of isotherm models (Langmuir and Freundlich) along with the correlation coefficients obtained by non-linear fitting method.

| Temperature (K) | Adsorption isotherm | Parameters | Value | |
|---|---|---|---|---|
| | | | $Pb^{+2}$ | $Cd^{+2}$ |
| 298 | Langmuir | $Q_{max}$ ($mg.g^{-1}$) | 342.76 | 171.21 |
| | | $K_L$ ($L.mg^{-1}$) | 0.022 | 0.028 |
| | | $R^2$ | 0.982 | 0.98 |
| | Freundlich | $K_F$ (($mg.g^{-1}$) ($mg.L^{-1}$)$^{-1/n}$) | 35.46 | 23.06 |
| | | n | 2.48 | 2.77 |
| | | $R^2$ | 0.935 | 0.933 |
| 303 | Langmuir | $Q_{max}$ ($mg.g^{-1}$) | 360.56 | 191.84 |
| | | $K_L$ ($L.mg^{-1}$) | 0.025 | 0.028 |
| | | $R^2$ | 0.988 | 0.991 |
| | Freundlich | $K_F$ (($mg.g^{-1}$) ($mg.L^{-1}$)$^{-1/n}$) | 40.56 | 24.16 |
| | | n | 2.55 | 2.67 |
| | | $R^2$ | 0.946 | 0.955 |
| 308 | Langmuir | $Q_{max}$ ($mg.g^{-1}$) | 376.48 | 204.54 |
| | | $K_L$ ($L.mg^{-1}$) | 0.026 | 0.032 |
| | | $R^2$ | 0.99 | 0.994 |
| | Freundlich | $K_F$ (($mg.g^{-1}$) ($mg.L^{-1}$)$^{-1/n}$) | 43.56 | 28.99 |
| | | n | 2.57 | 2.81 |
| | | $R^2$ | 0.944 | 0.969 |

**Table 4**
Thermodynamic parameters for $M^{2+}$ ion adsorption on the surface of the EDTA@PD-CNT/$Fe_3O_4$ adsorbent.

| $M^{2+}$ ion | $\Delta S^0$ | $\Delta H^0$ | Temperature | $K_d$ | $\Delta G^0$ | $R^2$ |
|---|---|---|---|---|---|---|
| | ($J.mol^{-1}.K^{-1}$) | ($KJ.mol^{-1}$) | (K) | ($L.g^{-1}$) | ($KJ.mol^{-1}$) | |
| $Pb^{+2}$ | 39.07 | 9.84 | 298 | 2.09 | −1.80 | 0.986 |
| | | | 303 | 2.25 | −1.99 | |
| | | | 308 | 2.38 | −2.19 | |
| $Cd^{+2}$ | 55.78 | 16.42 | 298 | 1.09 | −0.202 | 0.976 |
| | | | 303 | 1.24 | −0.481 | |
| | | | 308 | 1.36 | −0.76 | |

**Table 5**
Concentration mixtures of $Pb^{2+}$ and $Cd^{2+}$ ions (gray) in the binary absorption system study.

| | Concentration of $Pb^{2+}$ $mg.L^{-1}$ | | | | | |
|---|---|---|---|---|---|---|
| **Concentration of $Cd^{2+}$ $mg.L^{-1}$** | | 0 | 20 | 40 | 60 | 80 |
| | 0 | 0 | 20 | 40 | 60 | 80 |
| | 20 | 20 | 40 | 60 | 80 | 100 |
| | 40 | 40 | 60 | 80 | 100 | 120 |
| | 60 | 60 | 80 | 100 | 120 | 140 |
| | 80 | 80 | 100 | 120 | 140 | 160 |

### *2.9. Reusability*

The reusability and stability of the adsorbent were assessed using five consecutive adsorption-desorption experiments.

### *2.10. Evaluation of EDTA@PD-CNT/Fe3O4 adsorbent performance*

Ultimately, the efficacy of the synthesized adsorbent (EDTA@PD-CNT/$Fe_3O_4$) was evaluated by comparison with CNT, O-CNT, and M-CNT.

## 3. Result and discussion

### *3.1. Characterization of EDTA@PD-CNT/$Fe_3O_4$*

The crystal structures of the composites (CNT, M-CNT, and EDTA@PD-CNT/$Fe_3O_4$) were examined using wide-angle XRD spectra. The XRD pattern of the MWCNT (Fig. 2) reveals peaks at $2\theta = 26.05$ and $43.55^\circ$, which represent the 002 and 100 carbon atom planes, respectively [50]. The XRD pattern of M-CNT does not show any diffractions related to carbon nanotubes, but the Fe3O4 cubic sheet planes 220, 311, 400, 422, 511, and 440 are responsible for the highest diffraction at $2\theta = 30.40$, 35.70, 43.30, 53.70, 57.20, and

**Table 6**
Comparison of the maximum adsorption capacities of EDTA@PD-CNT/$Fe_3O_4$ with various adsorbents.

| Adsorbent | Target element | Isotherm | Kinetic | $Q_{max}$ ($mg.g^{-1}$) | Year | Ref. |
|---|---|---|---|---|---|---|
| EDTA@PD-CNT | $Cd^{+2}$ | Langmuir | PSO | 204.54 | – | This work |
| | $Pb^{+2}$ | | | 376.46 | | |
| $Fe_3O_4$@CS-EDTA | $Co^{+2}$ | Langmuir | PSO | 48.78 | 2019 | [30] |
| EDTA-Chitosan | $Co^{+2}$ | Sips | PSO | 61.00 | 2021 | [49] |
| | $Sr^{+2}$ | | | 8.80 | | |
| EDTA-mGO | $Pb^{+2}$ | Freundlich Temkin | PSO | 508.40 | 2015 | [35] |
| | $Hg^{+2}$ | | | 268.40 | | |
| | $Cu^{2+}$ | | | 301.2 | | |
| EFB | $Ca^{+2}$ | Langmuir | PSO | 26.50 | 2011 | [39] |
| | $Cd^{+2}$ | | | 41.00 | | |
| | $Pb^{+2}$ | | | 89.21 | | |
| Cell-EDTA | $Cd^{+2}$ | Langmuir | PSO | 48.02 | 2020 | [38] |
| | $Pb^{+2}$ | | | 63.92 | | |
| CTS/PAM gel | $Cu^{+2}$ | Langmuir | PSO | 99.44 | 2016 | [9] |
| | $Cd^{+2}$ | | | 86.00 | | |
| | $Pb^{+2}$ | | | 138.41 | | |
| $Fe_3O_4$-CS/EDTA | $Cu^{+2}$ | Langmuir | PSO | 225.00 | 2019 | [34] |
| | $Pb^{+2}$ | | | 220.00 | | |
| Mag-Ligand | $Cd^{+2}$ | Langmuir | PSO | 79.36 | 2015 | [31] |
| | $Pb^{+2}$ | Freundlich | | 100.20 | | |

62.80°, respectively [51]. Since ethylenediaminetetraacetic acid-functionalized polydopamine is amorphous, the XRD investigation of EDTA@PD-CNT/$Fe_3O_4$ does not reveal any novel diffraction patterns.

The FT-IR spectra depicted in Fig. 3 analyze the vibrational characteristics of the functional groups present in the CNT, O-CNT, M-CNT, and EDTA@PD-CNT/$Fe_3O_4$. The broad peak in the range of 3300–3600 $cm^{-1}$ corresponds to the vibrational frequencies of the O-H bond, while the two peaks seen at 2856 and 2925 $cm^{-1}$ are associated with the vibrational frequencies of the aliphatic C-H bonds [52]. The absorption bands at 1573, 1641, and 1720 $cm^{-1}$ seen in all samples, except for EDTA@PD-CNT/$Fe_3O_4$, can be attributed to the vibrations of the C=C and C=O bonds in carbon nanotubes, respectively [53,54]. The presence of a peak at 588 $cm^{-1}$ in the M-CNT sample can be attributed to the vibrational frequency of the Fe-O bond, suggesting the successful synthesis of $Fe_3O_4$ particles in this sample [55]. The successful synthesis of polydopamine modified with ethylenediaminetetraacetic acid can be proved by new peaks appearing in the spectrum of EDTA@PD-CNT/$Fe_3O_4$. The range of 1530–1690 $cm^{-1}$ in the spectrum of EDTA@PD-CNT/$Fe_3O_4$ corresponds to the vibrational frequency of the carbonyl group (C=O) in the amide and acidic residues, as well as N-H bending [56]. The stretching vibrations of the C-N and C-O bond appeared at 1296 $cm^{-1}$ and 1126 $cm^{-1}$, respectively. The peak observed at 1384 $cm^{-1}$ can be attributed to the symmetric stretching vibrations of the carboxylate group ($-COO^-$) [34,57]. The peak observed at 1471 $cm^{-1}$ can be attributed to the C=C of the aromatic rings. A combination of field emission scanning electron microscopy (FE-SEM) and energy dispersive spectroscopy (EDS) was employed to examine the physical and chemical alterations occurring in CNTs. Fig. 4 displays the images associated with the synthesized samples. The first image shows the tubular structure of carbon nanotubes, which is a suitable choice for making composites. The change observed in the morphology of carbon nanotubes, and the percentage of their chemical composition after oxidation can be seen in the image associated with the O-CNT sample. As seen in the FE-SEM image of the composite containing $Fe_3O_4$ nanoparticles, the gathering of the CNT filaments with $Fe_3O_4$ nanoparticles has considerably changed the morphology of the solid, and perhaps the porosity of the solid has been affected to a large extent; this has been discussed in the following paragraphs ($N_2$ adsorption-desorption analysis). Finally, the FE-SEM image of the final composite, i.e., EDTA@PD-CNT/-$Fe_3O_4$, shows the formation of homogeneous polydopamine shells around the M-CNT [58]. The alteration in the structure and composition of carbon nanotubes validate the successful creation of magnetic nanoparticles and polydopamine on the surface of the CNTs. Furthermore, the rise in the proportion of nitrogen (4.12 %) and oxygen (20.65 %) in the produced composite serves as evidence of the successful creation of EDTA@PD-CNT/$Fe_3O_4$ as an intendant adsorbent. Fig. 5 displays the FE-SEM-EDS mapping of the EDTA@PD-CNT/$Fe_3O_4$ composite and its corresponding structural components. The existence of EDTA@PD in the final adsorbent is confirmed by the presence of oxygen and nitrogen atoms in the composite.

The addition of $Fe_3O_4$ is very important for operationally easily separating adsorbent from an aqueous solution. The presence of $Fe_3O_4$ nanoparticles in the adsorbent confers magnetism, enabling rapid separation with the use of an external magnet. The magnetic hysteresis line of EDTA@PD-CNT/$Fe_3O_4$ in Fig. 6 demonstrates that the suggested adsorbent possesses magnetic characteristics, exhibiting a saturation magnetization of 17.66 emu/g. Magnetic separation is a cost-effective and time-saving method for the adsorption process [59]. Variations in zeta potential were assessed at various pH levels to examine the surface charge of the EDTA@PD-CNT/Fe3O4 composite. The outcomes of this examination are displayed in Fig. 7. The pH of the solution has a big impact on the surface charge of EDTA@PD-CNT/$Fe_3O_4$ because it has many functional groups, such as hydroxyl (-OH) and carboxyl (-COOH) groups. Since the $pH_{ZPC}$ of the adsorbent is about 5.34 and since the surface of the adsorbent becomes negative at a pH higher than the $pH_{ZPC}$, it can be concluded that EDTA@PD-CNT/$Fe_3O_4$ is a suitable alternative for the adsorption of cationic contaminants.

The thermal stabilities of CNT, O-CNT, M-CNT, and EDTA@PD-CNT/$Fe_3O_4$ composites were measured by thermogravimetric analysis. Diagrams of the thermogravimetric analysis (TGA) and differential thermal analysis (DTA) are shown in Fig. 8(a and b). In

**Table 7**
Adsorption equations, nonlinear equations of kinetics, nonlinear equations of isotherms, thermodynamic equations, and their corresponding parameters.

| Models | Equations | Parameters (unit) |
|---|---|---|
| (1) Adsorption equations | (a) $Q_t = \frac{(C_0 - C_t)V}{m}$ (b) $Q_e = \frac{(C_0 - C_e)V}{m}$ (c) $\%Removal = \frac{(C_0 - C_e)}{C_0} \times 100$ | $Q_e$: Equilibrium adsorption capacity (mg.g$^{-1}$)<br>$Q_t$: Adsorption capacity at time t (mg.g$^{-1}$)<br>$C_0$: Initial concentration (mg.L$^{-1}$)<br>$C_t$: Residual concentration (mg.L$^{-1}$)<br>$C_e$: Equilibrium concentration (mg.L$^{-1}$)<br>V: Volume of heavy metal ion solution (mL)<br>m: Dosage of adsorbent (g) |
| (2) PFO | $Q_t = Q_{e,cal.}.\left(1 - e^{-k_1^{-1}.t}\right)$ | $Q_t$: Adsorption capacity at time t (mg g$^{-1}$)<br>$Q_{e,cal}$: Calculated adsorption capacity (mg g$^{-1}$)<br>t: Contact time (min)<br>$k_1$: Rate constant corresponding to pseudo-first-order (min$^{-1}$) |
| (3) PSO | $Q_t = \frac{Q_{e,cal.}^2.k_2.t}{1 + Q_{e,cal}.C_e}$ | $Q_t$: Adsorption capacity at time t (mg g$^{-1}$)<br>$Q_{e,cal}$: Calculated adsorption capacity (mg g$^{-1}$)<br>$k_2$: rate constants corresponding to pseudo-second-order (g.mg$^{-1}$.min$^{-1}$)<br>$C_e$: Equilibrium concentration (mg.L$^{-1}$)<br>t: Contact time (min) |
| (4) Elovich | $Q_t = \frac{1}{\beta}.\ ln(\alpha.\beta).t$ | $Q_t$: Adsorption capacity at time t (mg g$^{-1}$)<br>α: Initial adsorption rate (mg.g$^{-1}$.min$^{-1}$)<br>β: Desorption constant during each experiment (g.mg$^{-1}$)<br>t: Contact time (min) |
| (5) IPD | $Q_t = k_{diff}.t^{\frac{1}{2}} + C$ | $Q_t$: Adsorption capacity at time t (mg.g$^{-1}$)<br>$k_{diff}$: IPD rate constant (mg.g$^{-1}$min$^{-1/2}$)<br>t: Contact time (min)<br>C: Intercept (thickness of the boundary layer) (mg.g$^{-1}$) |
| (6) Langmuir | $Q_e = \frac{Q_{e.Max}.K_L.C_e}{1 + (K_L.C_e)}$ | $Q_e$: Equilibrium adsorption capacity (mg.g$^{-1}$)<br>$Q_{e.Max}$: Maximum equilibrium adsorption capacity (mg.g$^{-1}$)<br>$C_e$: Equilibrium concentration (mg.L$^{-1}$)<br>$K_L$: Langmuir constant (L.mg$^{-1}$) |
| (7) Freundlich | $Q_e = K_F.C_e^{\frac{1}{n}}$ | $Q_e$: Equilibrium adsorption capacity (mg.g$^{-1}$)<br>$C_e$: Equilibrium concentration (mg.L$^{-1}$)<br>$K_F$: Freundlich constant associated with adsorption capacity. (mg.g$^{-1}$) (mg. L$^{-1}$)$^{-1/n}$<br>n: Freundlich constants associated with adsorption intensity. |
| (9) Thermodynamic equations | $\Delta G^0 = \Delta H^0 - T\Delta S^0$ | $\Delta G^0$: Gibbs free energy of adsorption (J.mol$^{-1}$)<br>$\Delta H^0$: Enthalpy of adsorption (J.mol$^{-1}$)<br>$\Delta S^0$: Entropy of adsorption (J.mol$^{-1}$.K$^{-1}$)<br>T: Temperature (K) |
| (10) | $Ln\ K_d = \frac{\Delta S^0}{R} - \frac{\Delta H^0}{R.T}$ | R: 8.314 J mol$^{-1}$ K$^{-1}$<br>$K_d$: Equilibrium constant (L.g$^{-1}$)<br>$K_d = \frac{Q_e}{C_e}$ |

Fig. 8 (a), the weight loss was observed around 600 °C for CNT and O-CNT due to the destruction of the carbon nanotube structure. In the graph related to M-CNT, the weight loss of roughly 40 % can be related to the disintegration of the carbon nanotube structure. The addition of $Fe_3O_4$ nanoparticles in the M-CNT enhances the thermal capacity of the composite, and in this respect, the degradation of the carbon nanotube structure occurs at lower temperatures (approximately 400 °C). Also, the catalytic action of $Fe_3O_4$ can is helpful in the breakdown of carbon skeleton [37,60]. The linear trend observed in the graph of M-CNT, starting at 600 °C, provides evidence for the presence of a $Fe_3O_4$ mineral compound. The weight loss below 200 °C in the graph related to EDTA@PD-CNT/$Fe_3O_4$ can be related to the loss of adsorbed water in the composite structure. The decomposition of the composite organic coating starts at a temperature of around 200 °C with decarboxylation and is completed by the decomposition of CNTs at about 600 °C. Therefore, the organic portion (polydopamine modified with EDTA) is anticipated to be around 51 %, $Fe_3O_4$ nanoparticles about 31 %, and carbon nanotubes about 11 % in the final composite. The changes observed in DTA (Fig. 8 (b)) are completely consistent with the changes in TGA (Fig. 8 (a)). Therefore, it can be concluded that phase changes did not occur in the samples, and all the changes are related to the reduction of the mass of the samples. The presence of broad peaks in the DTA diagram shows thermal decomposition during temperature changes.

Nitrogen gas adsorption-desorption along with pore size distribution (BJH analysis) of the CNT, O-CNT, M-CNT, and EDTA@PD-CNT/$Fe_3O_4$ were investigated (Fig. 9(a–d)). As to the IUPAC classification, the adsorption isotherm exhibits characteristics similar to type IV isotherms, with a small hysteresis loop [61]. Since the hysteresis loop cannot help in confirming the structure, it is perhaps difficult to confirm the mesoporous structure; however, the adsorption at the $P/P_0$ of 0.8–1 can be attributed to the adsorption between the void volumes of the nanoparticles. As a result, adsorption with a small hysteresis loop can be related to compounds with micro-mesoporous morphology [62]. The change in the BJH diagram of M-CNT and EDTA@PD-CNT/$Fe_3O_4$ samples compared to CNT and O-CNT samples shows the change in their textural characteristics. The Brunauer-Emmett-Teller (BET) equation and nitrogen adsorption and desorption diagram were used to find the specific surface area of all samples. The results are displayed in Table 1.

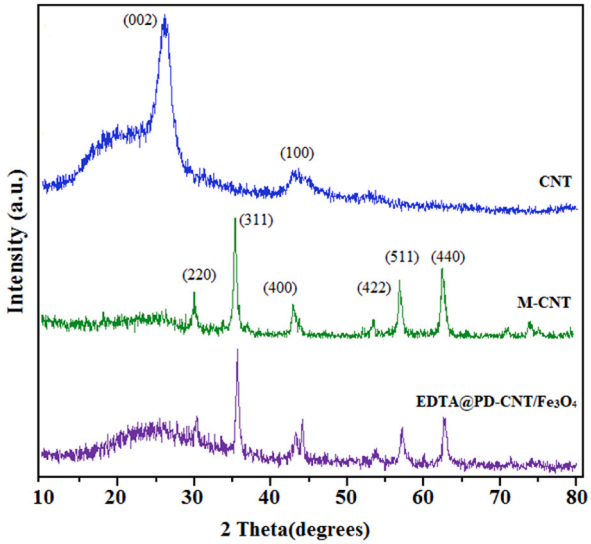


**Fig. 2.** X-ray diffraction pattern of the samples CNT, M-CNT, EDTA@PD-CNT/$Fe_3O_4$.

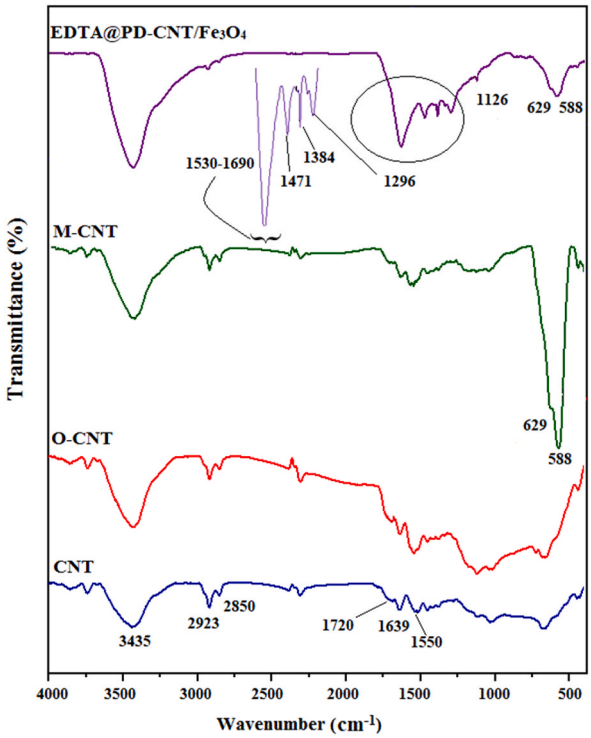


**Fig. 3.** FT-IR spectra of the samples CNT, O-CNT, M-CNT, EDTA@PD-CNT/$Fe_3O_4$.

Although the total pore volume and surface area of the final composite are reduced, the mean pore diameter does not change significantly compared to carbon nanotubes. The surface area of EDTA@PD-CNT/$Fe_3O_4$ is reduced because polydopamine functionalized with EDTA covers the surface area of the CNTs. Although the surface area was reduced, functional groups with chelating properties were increased on the surface, hence raising the $Cd^{+2}$ and $Pb^{+2}$ ion adsorption abilities. Adsorption capacity results under optimal conditions for CNT, O-CNT, M-CNT, and EDTA@PD-CNT/$Fe_3O_4$ are shown in Fig. 16.

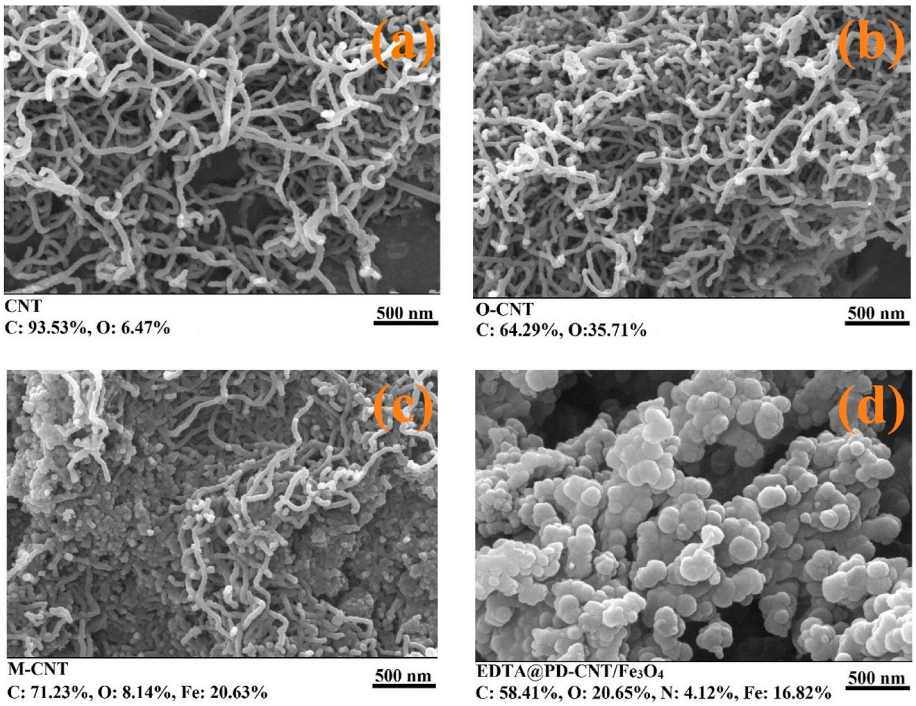


**Fig. 4.** The FE-SEM images with the EDX results of the CNT(a), O-CNT(b), M-CNT(c), EDTA@PD-CNT/$Fe_3O_4$(d) samples.

### 3.2. Effect of pH on the removal efficiency

The influence of pH on the process of surface adsorption of heavy metal ions is not hidden from anyone. This study examined the effect of pH on the adsorption of $Cd^{2+}$ and $Pb^{2+}$ ions by the EDTA@PD-CNT/$Fe_3O_4$ composite through a series of experiments. The pH of the solutions has been modified to a range of 2–7 for the purpose of these experiments because a pH above 6 leads to unfavorable adsorption processes due to the precipitation of $Cd^{2+}$ and $Pb^{2+}$ hydroxides. Fig. 7 shows the change in zeta potential for the EDTA@PD-CNT/$Fe_3O_4$ adsorbent based on pH changes (in the range of 2–8). The $pH_{ZPC}$ for this composite was obtained at 5.34, indicating that the adsorbent content at this pH is uncharged. At pH < $pH_{ZPC}$, the hydroxyl (-OH) and carboxyl (-COOH) groups of the adsorbent are mostly protonated, leading to a positively charged surface, and thus the removal efficiency is low due to electrostatic repulsion. As can be seen (Fig. 10(a)), at pH = 2, the removal efficiency is negligible, and the removal efficiency increases by increasing the pH to 4. The adsorption at pH < $pH_{ZPC}$ can be related to the creation of hydrogen bonds between the solvent-coated ions and the polar groups on the surface of the EDTA@PD-CNT/$Fe_3O_4$ adsorbent. These groups are related to the hydroxyl groups found in $Fe_3O_4$ nanoparticles, polydopamine, oxidized CNTs, and the residual EDTA molecules. The optimal pH for achieving maximum removal efficiency was determined to be six for both $Cd^{2+}$ and $Pb^{2+}$ ions. At this pH, almost all the carboxylate and amine groups in the EDTA sites would be ready to anchor the $M^{2+}$ ions. Furthermore, when the pH > $pH_{ZPC}$, the adsorbent's surface charge becomes negative [35]. This leads to strong electrostatic attraction between positive ions and the adsorbent's surface, which contributes to its high adsorption capacity. These findings are consistent with the Zeta potential measurements. The adverse effects at pH = 7 compared to pH = 6 can be attributed to the creation of metal hydroxide [38,49]. To further investigate and control the effective parameters in the adsorption process of $Cd^{2+}$ and $Pb^{2+}$ ions, pH = 6 was chosen as optimal.

### 3.3. Effect of dosage on the removal efficiency

Once the proper pH of the $Cd^{2+}$ and $Pb^{2+}$ solutions was established, the adsorption process was examined at varying dosages of the EDTA@PD-CNT/$Fe_3O_4$ composite. Accurately determining the optimal dosage of adsorbent can effectively minimize expenses and waste. According to Fig. 10 (b), the removal efficiency of $Cd^{2+}$ ions escalated from 46.8 % to 92.0 % when the adsorbent dose was raised from 3 mg to 8 mg. For $Pb^{2+}$ ions, the removal efficiency rose from 50.0 % to 96.0 % when the dosage was escalated from 3 mg to 5 mg. There was no noticeable alteration in the removal efficiency when the adsorbent dose was further escalated. Increasing the adsorbent dosage increases the quantity of active adsorption sites on the adsorbent's surface, resulting in higher removal efficiency. These changes show that the maximum adsorption capacity is obtained in the appropriate dose of the adsorbent in such a way that the surface of the adsorbent is saturated with a certain concentration of heavy metal ions, and no significant change in the removal efficiency is observed [63].

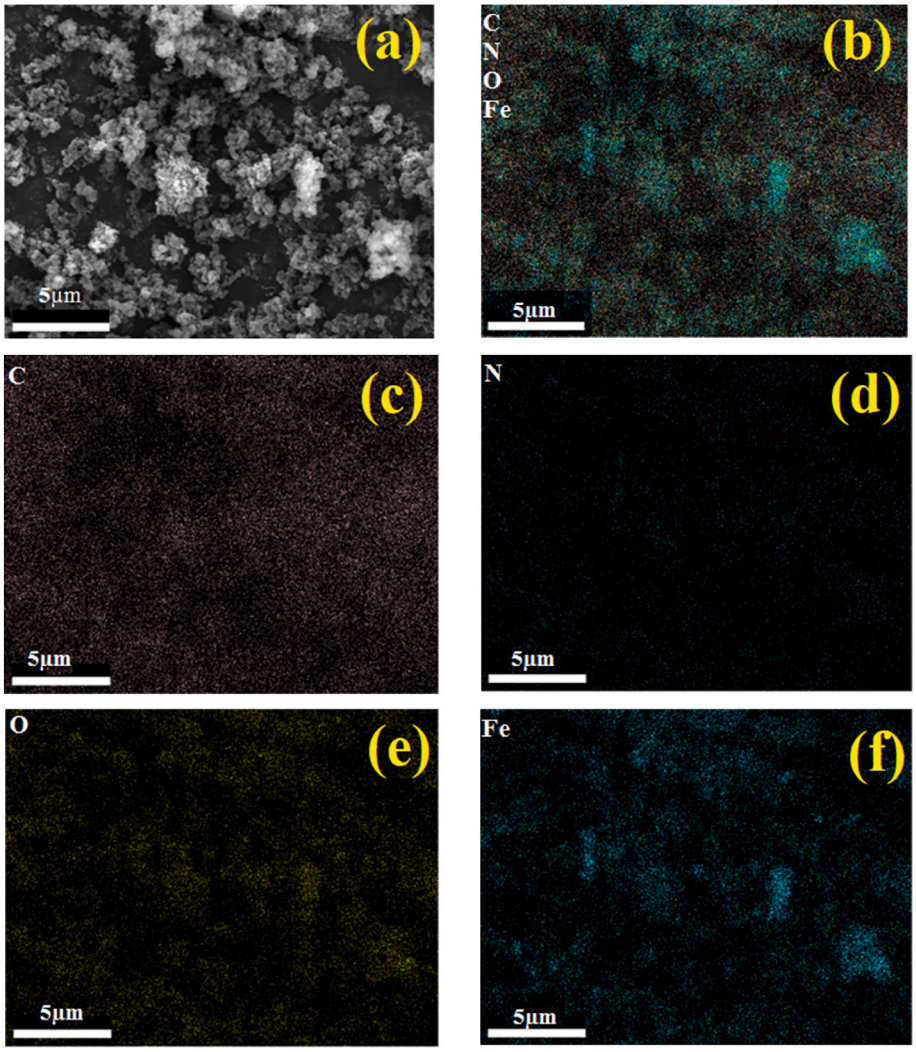


**Fig. 5.** FESEM image of the EDTA@PD-CNT/$Fe_3O_4$ sample (a), and EDX mapping of the EDTA@PD-CNT/$Fe_3O_4$ and the corresponding elements (b–f).

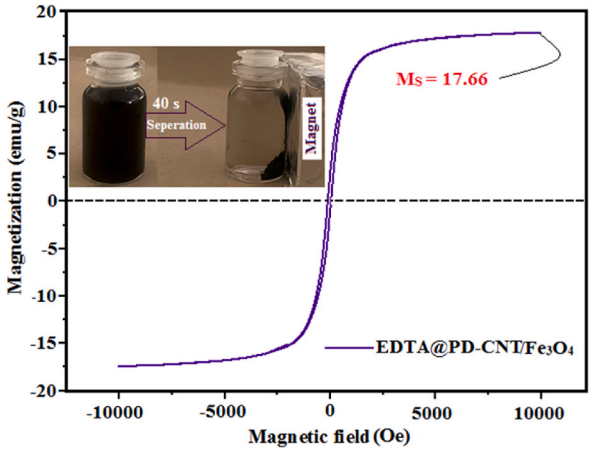


**Fig. 6.** Magnetization curve of sample EDTA@PD-CNT/$Fe_3O_4$.

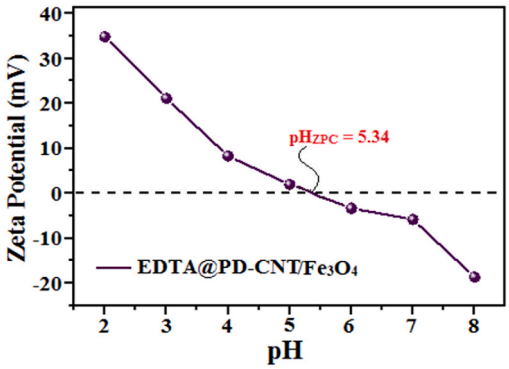


**Fig. 7.** Zeta potential analysis of sample EDTA@PD-CNT/$Fe_3O_4$.

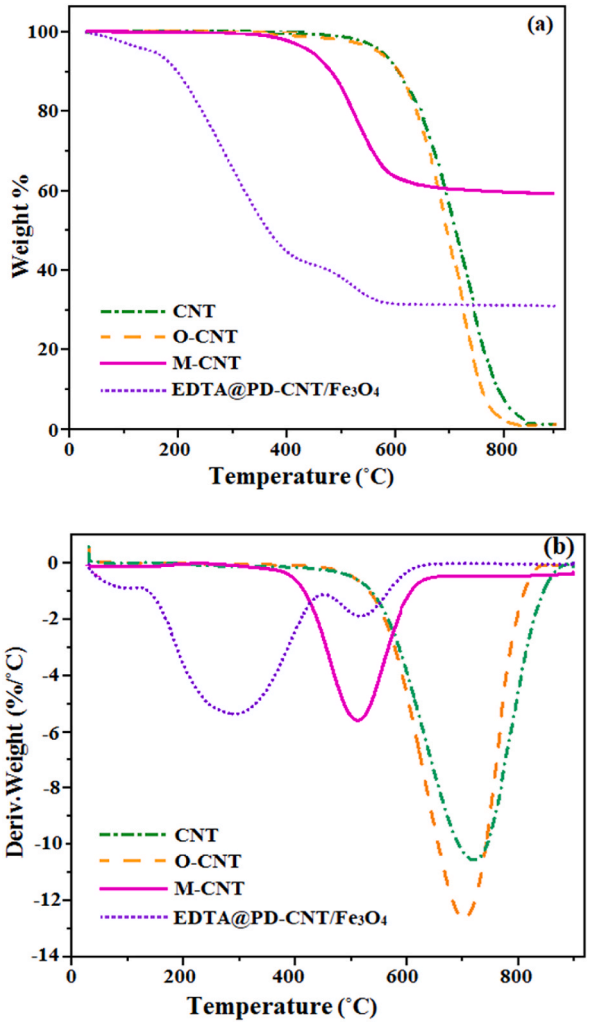


**Fig. 8.** TGA analysis (a) and DTA curves (b) of the CNT, O-CNT, M-CNT, and EDTA@PD-CNT/$Fe_3O_4$.

### *3.4. Effect of reaction time and investigation of adsorption kinetics*

The time needed to reach adsorption equilibrium is a crucial economic element in wastewater treatment. Reaction time studies were conducted for $Cd^{2+}$ (8 mg dosage, pH = 6, T = 298 K, 50 ppm) and $Pb^{2+}$ (5 mg dosage, pH = 6, T = 298 K, 50 ppm). The findings

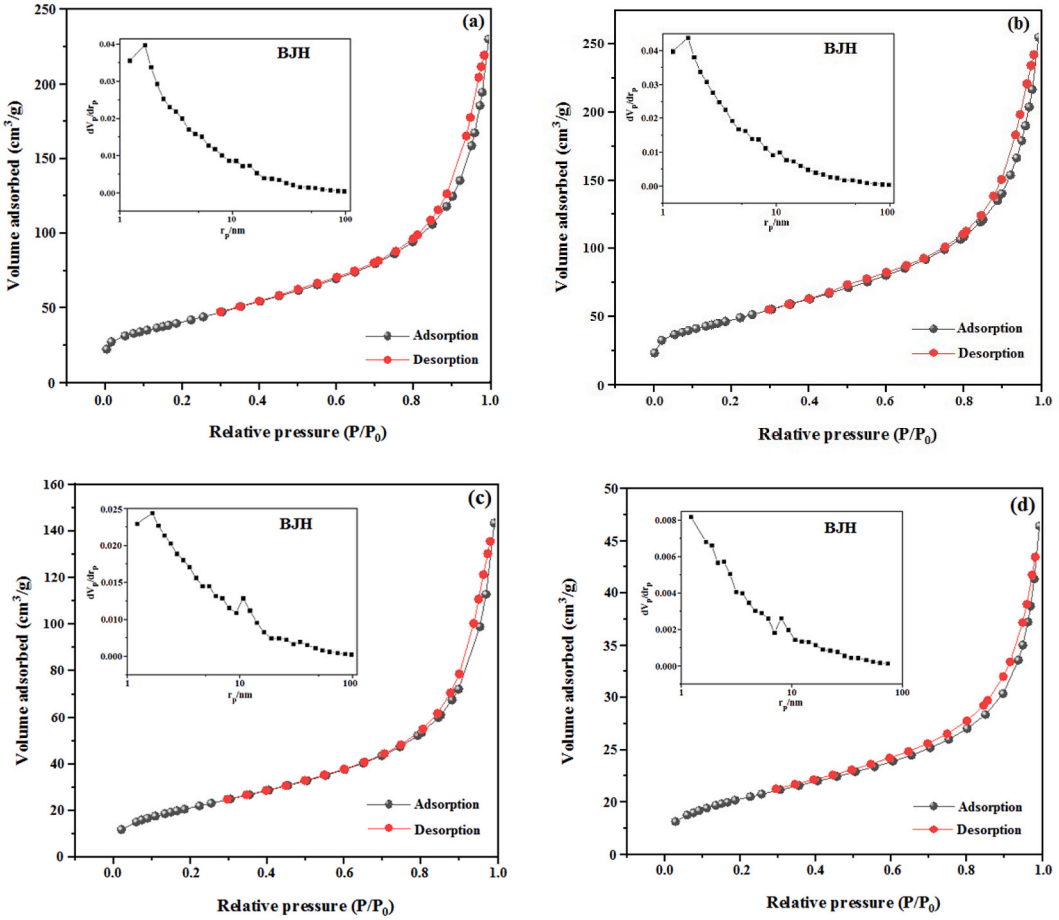


**Fig. 9.** $N_2$ adsorption-desorption isotherm and BJH curves (inset) of the samples CNT (a), O-CNT (b), M-CNT (c), EDTA@PD-CNT/$Fe_3O_4$ (d).

derived from this investigation are displayed in Fig. 11 (a) for both ions. The significant rise in adsorption capacity within the first 50 min before reaching equilibrium can be attributed to the high gradient of concentration at the interface between the adsorbent and the solution, as well as the presence of many surface-active sites [49]. Following 50 min and attaining equilibrium, there was no notable increase in adsorption capacity. The method of non-linear curve fitting analysis was utilized to examine the kinetics of adsorption and determine the kinetic parameters. The experimental data were analyzed using the pseudo-first-order (Eq. (2), Table 7), pseudo-second-order (Eq. (3), Table 7), and Elovich (Eq. (4), Table 7) kinetic models. The study calculated the kinetic parameters associated with each model and recorded the findings in Table 2. The reported results indicate that the pseudo-second-order model had a greater correlation coefficient ($R^2$) compared to the other two kinetic models that were examined. Furthermore, the $Q_{e.cal}$ calculated using this model exhibited a greater level of closeness to the experimental value ($Q_{exp}$). Also, the results in Table 2 indicate that in the pseudo-first-order kinetic model, $Q_{e.cal}$ is less than $Q_{exp.}$ The $R^2$ for this model is smaller than that of the pseudo-second-order and Elovich models. Thus, this model is unsuitable for describing the kinetic behavior of ions. Hence, the pseudo-second-order model well characterizes the adsorption kinetics of $Cd^{2+}$ and $Pb^{2+}$ on the adsorbent surface. Research demonstrates that the rate-limiting step is the chemisorption of ions on the adsorbent surface. The intra-particle diffusion (IPD) kinetics model (Eq. (5), Table 7) was employed to ascertain the rate-limiting step and precise mechanism of adsorption. The diagram of this investigation is depicted in Fig. 11 (b). If the graph represents a linear relationship that intersects the origin, it can be inferred that the adsorption is governed by the kinetics of intra-particle diffusion and that the boundary layer has a negligible thickness. However, as depicted in Fig. 11(b), each segment of the curve is split into two lines, each characterized by distinct values of $R^2$ and rate constant. The first step, which has a rate constant of $k_{i1}$, is caused by adsorption on the adsorbent's surface and mass transfer from outside the system [64]. The second step, characterized by a rate constant of $k_{i2}$, is associated with the slow adsorption process occurring on the adsorbent's surface. As the concentration of ions in the solution declines and the adsorbent surface gets saturated, the diffusion resistance increases with time. Therefore, as seen in Table 2, $k_{i2}$ is smaller than $k_{i1}$ [65].

### 3.5. *Effect of the concentration and adsorption isotherms*

It is crucial to examine the impact of $Cd^{2+}$ and $Pb^{2+}$ ion concentrations on the adsorption process, determine the maximum

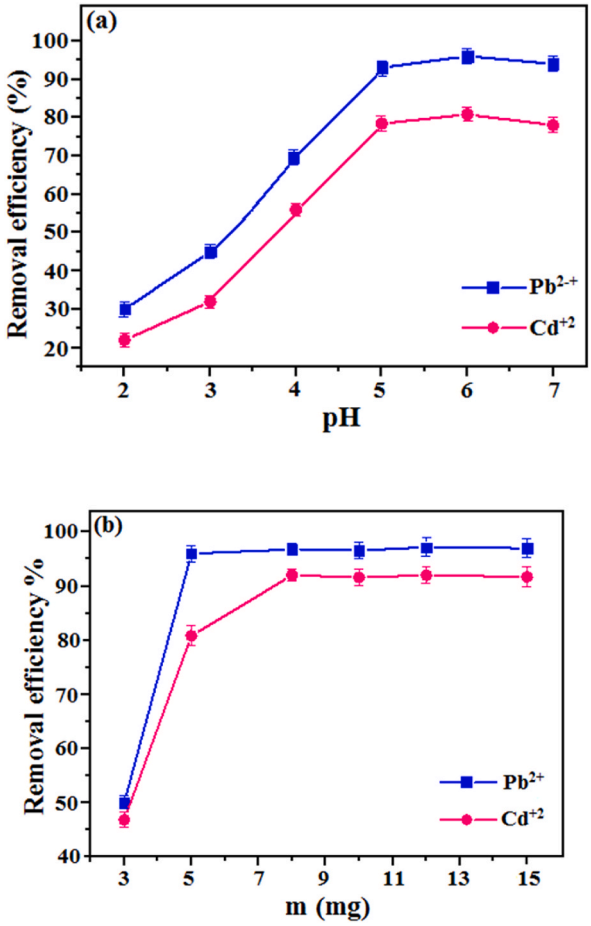


**Fig. 10.** The influence of solution pH (a) and adsorbent dose (b) on the adsorption process of $Cd^{2+}$ and $Pb^{2+}$ by the EDTA@PD-CNT/$Fe_3O_4$.

adsorption capacity, understand how metal ions and the adsorbent's surface interact, and ultimately gain a comprehensive understanding of the adsorption mechanism. Fig. 12 (a–b) shows the effects of $Cd^{2+}$ and $Pb^{2+}$ ion concentrations utilizing the EDTA@PD-CNT/$Fe_3O_4$ adsorbent in ideal conditions and at three different temperatures. The first increase can be attributed to the elevated concentration of metal ions, subsequently accompanied by a substantial driving force to tackle the mass transfer [66]. Once equilibrium is reached, any further rise in the initial concentration will not result in a significant increase in the adsorption capacity. The cause can be ascribed to the saturation of active sites on the surface of the adsorbent. The highest adsorption capacity achieved for $Cd^{2+}$ and $Pb^{2+}$ ions at 45 °C was 204.54 mg $g^{-1}$ and 376.48 mg $g^{-1}$, respectively. The results obtained from EDTA-terminated adsorbents are compared with these values in Table 4. Next, we employed the Langmuir and Freundlich isotherm models to simulate experimental data. The non-linear relationships of Langmuir and Freundlich isotherms are expressed by Eqs. (6) and (7) in Table 7, respectively. The parameters derived from the Langmuir and Freundlich isotherms, along with the non-linear correlation coefficient ($R^2$), are presented in Table 3. The comparison of $R^2$ values between the Langmuir and Freundlich models indicates that the Langmuir model has a greater $R^2$ value across three distinct temperatures. In addition, the Langmuir model yields a maximum saturation adsorption capacity ($Q_{max}$) that closely matches the experimental observations. The findings indicate that the chemical adsorption process of lead and cadmium ions on the EDTA@PD-CNT/$Fe_3O_4$ adsorbent surface takes place as a monolayer. Furthermore, based on the appropriateness of the Langmuir model in explaining the adsorption process of EDTA@PD-CNT/Fe3O4, it can be inferred that the uniformity of the adsorbent surface is a result of the presence of identical adsorption sites. The values of n ranging from 1 to 10 for the Freundlich isotherm suggest that the modified adsorbent exerted a significant influence on ions [67].

Ultimately, to assess the reliability of the adsorption process, the $R_L$ parameter was computed using Eq. (8). A value between 0 and 1 for $R_L$ signifies a favorable adsorption process and an appropriate adsorbent [68]. Fig. 13 (a) shows the trend curve of the dimensionless separation factor ($R_L$) for $Cd^{2+}$ and $Pb^{2+}$ ions using EDTA@PD-CNT/$Fe_3O_4$ adsorbent. According to this study, $R_L$ has a value between 0 and 0.8. Consequently, the $Cd^{2+}$ and $Pb^{2+}$ ions adsorption on the EDTA@PD-CNT/$Fe_3O_4$ surface is favorable [69]. The equation involves the Langmuir constant, $K_L$ (L.$mg^{-1}$), and the initial concentration of ions, $C_0$ (mg.$L^{-1}$).

$$R_L = \frac{1}{1 + K_L C_0} \tag{8}$$

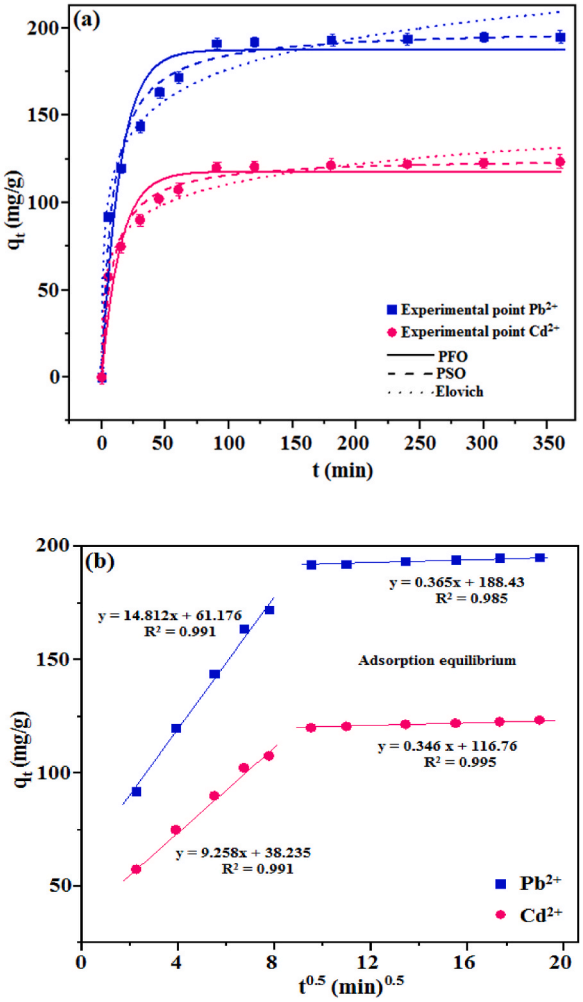


**Fig. 11.** Kinetic non-linear fitting of EDTA@PD-CNT/$Fe_3O_4$ for $Pb^{+2}$ and $Cd^{+2}$ adsorption (a), investigating the intra-particle diffusion model (b), $Pb^{+2}$ (dosage = 5 mg, pH = 6, T = 298K, 50 ppm) and $Cd^{+2}$ (dosage = 8 mg, pH = 6, T = 298K, 50 ppm).

### 3.6. *Effect of temperature and thermodynamics analysis*

The experiments were performed to examine the impact of temperature on the adsorption process and obtain thermodynamic parameters. Fig. 12 (a–b) demonstrates that raising the temperature from 25 °C to 45 °C results in an increased number of encounters between metal ions and the adsorbent surface. Raising the temperature can also aid in the deprotonation of the carboxylic acid groups present on the surface, increasing the number of adsorption sites [66]. Table 3 shows that the maximum adsorption capacity at a temperature of 25 °C was achieved for $Cd^{2+}$ and $Pb^{2+}$ ions, with values of 171.21 and 342.76 mg $g^{-1}$, respectively. Notably, the results exhibited a positive correlation with rising temperature for both ions. To further investigate and understand the mechanisms more precisely, thermodynamic parameters were measured for both $Cd^{2+}$ and $Pb^{2+}$ ions. Thermodynamic relations along with parameters are presented by equations (9) and (10) in Table 7. A linear plot of $K_d$ versus 1/T was first plotted (Fig. 13 (b)). $K_d$ is the equilibrium constant obtained from Eq. (11), where $Q_e$ (mg.$g^{-1}$) and $C_e$ (mg.$L^{-1}$) represent the adsorption capacity and concentration at the adsorption equilibrium point, respectively.

$$K_d = \frac{Q_e}{C_e} \tag{11}$$

Table 4 displays the outcomes of linear regression. The correlation coefficient ($R^2$) about the thermodynamic diagrams of both examined ions exceeds 0.96, indicating a high degree of proximity between the experimental and theoretical values. The spontaneous nature of the adsorption process is indicated by the negative change in standard free Gibbs energy ($\Delta G^\circ$) at various temperatures. The values that are positive for the standard enthalpy change ($\Delta H^\circ$) and standard entropy change ($\Delta S^\circ$) suggest that the adsorption of $Cd^{2+}$ and $Pb^{2+}$ ions on the adsorbent surface is a process that absorbs heat from the surrounding environment (endothermic process) and is

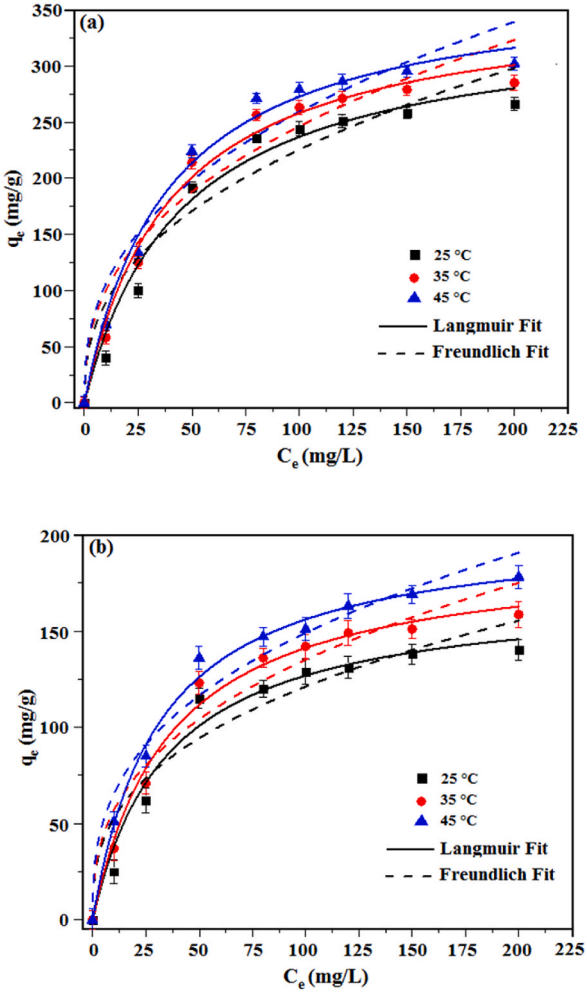


**Fig. 12.** Non-linear isotherm curve of EDTA@PD-CNT/$Fe_3O_4$ for $Pb^{2+}$ (a) and $Cd^{2+}$ (b) adsorption at various temperatures.

an entropy-driven process [69].

### 3.7. Evaluating the efficiency of the adsorbent in the binary adsorption system

This work aimed to examine the behavior of the EDTA@PD-CNT/$Fe_3O_4$ adsorbent in a binary adsorption system. Initially, solutions were created that consisted of a combination of $Pb^{2+}$ and $Cd^{2+}$ ions (as indicated in Table 5, gray section). The pH of all solutions was set to 6. Subsequently, the adsorbent was added, and the samples were agitated at room temperature for 2 h at a rate of 200 rpm. The adsorbent was isolated from the solution using a magnet, and the concentration of the residual ions was determined. Fig. 14 (a) and 14 (b) display the contour diagrams associated with $Pb^{2+}$ and $Cd^{2+}$ ions. Because there are only a limited number of places where ions can be adsorbed, they must compete with each other to be adsorbed onto the surface of the adsorbent. Consequently, the adsorbent will adsorb the ion that has a greater affinity for adsorption [49]. The adsorption behavior of ions in mixed environments can be explained by employing the covalent index (Eq. (12)). The parameter "r" represents the atomic radius, whereas "$E_n$" reflects the electronegativity value of the ion under investigation. $Pb^{2+}$ has a larger atomic radius and higher electronegativity compared to $Cd^{2+}$, resulting in a rise in the covalent index. The higher the covalent index of an ion, the stronger the adsorbent's affinity for adsorbing that particular species [38]. The result about the efficacy of adsorbent in removing the mixture of $Pb^{2+}$ and $Cd^{2+}$ ions indicates that $Pb^{2+}$ exhibited an improved uptake compared to $Cd^{2+}$.

$$\text{Covalent index} = (E_n)^2 r \tag{12}$$

### 3.8. Reusability

One of the essential features of a high-quality and cost-effective adsorbent is its reusability. For this study, firstly, the EDTA@PD-

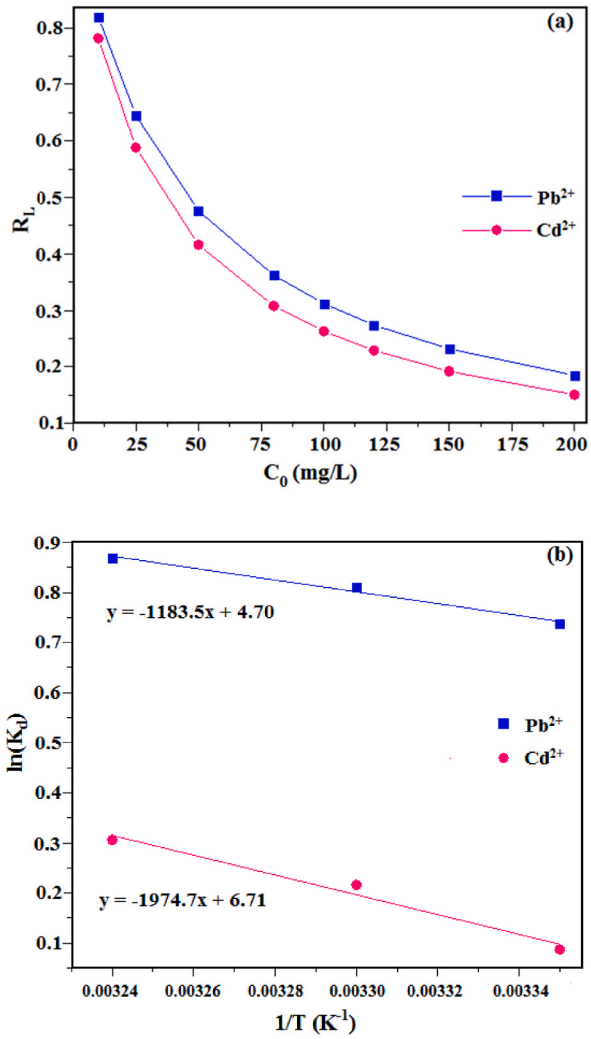


**Fig. 13.** $R_L$ trend curve (a) and Arrhenius plot of ln ($K_d$) vs 1/T (b).

CNT/$Fe_3O_4$ adsorbent was separated by a magnetic field after being used once in the adsorption experiment. Subsequently, the adsorbent was washed using a 0.5 M hydrochloric acid solution to eliminate the adsorbed ions. Subsequently, it was washed with water and made ready for further utilization. The adsorbent was used for four additional cycles, and the percentage removal was calculated at each step. Fig. 15 (a) and 15 (b) show the results of $Pb^{2+}$ and $Cd^{2+}$ adsorption and desorption, respectively. It is known that the amount of $Pb^{2+}$ removal efficiency reduced from 96 % to 80.7 %, and the amount of $Cd^{2+}$ removal efficiency reduced from 92 % to 80 % after five uses. The results show the reusability and cost-effectiveness of the EDTA@PD-CNT/$Fe_3O_4$ adsorbent.

### *3.9. Evaluation of EDTA@PD-CNT/Fe3O4 adsorbent performance*

The experiments investigated the impact of oxygen and nitrogen functional groups in the EDTA molecule on adsorption. CNT, O-CNT, M-CNT, and EDTA@PD-CNT/$Fe_3O_4$ were employed as adsorbents under optimal conditions of temperature (298 K), time (90 min), pH = 6, volume (20 mL), and concentration (100 ppm). The dosage of the investigated adsorbents for the removal of $Pb^{2+}$ was 5 mg, whereas for $Cd^{2+}$, it was 8 mg. The samples underwent agitation using a reciprocating shaker bath at a temperature of 25 °C and a speed of 200 rpm for 2 h. Subsequently, the ion concentration in all samples was measured using atomic absorption spectroscopy, and the removal efficiency was computed. The results of this study are depicted in Fig. 16. Despite the reduction in surface area due to CNT surface modification, the removal efficiency of EDTA@PD-CNT/$Fe_3O_4$ has dramatically increased (over 90 %) compared to CNT. The rise can be related to the presence of EDTA and the increase of active adsorption sites on the CNT surface.

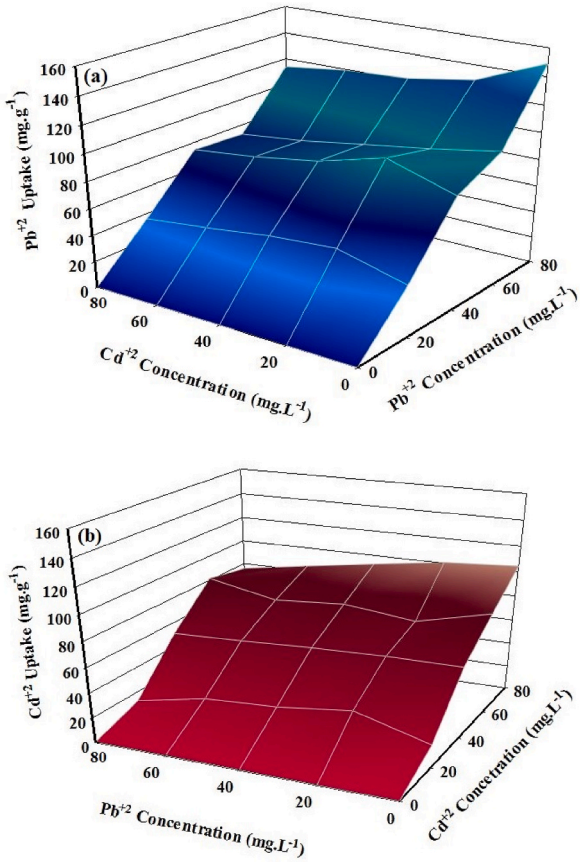


**Fig. 14.** Contour diagrams related to the adsorption of $Pb^{2+}$ (a) and $Cd^{2+}$ (b) ions in the binary adsorption system at room temperature, pH = 6, and duration of 2 h.

### *3.10. Adsorption mechanism*

The analysis of the thermodynamics, kinetics, and isotherms of adsorption in the preceding sections revealed that the adsorption of ions onto the adsorbent surface follows a monolayer mechanism involving chemical interactions and is characterized by an endothermic process. Section 3.9 examined the efficacy of the ultimate adsorbent and the impact of EDTA on the adsorption. The findings demonstrated that EDTA plays a significant role in effectively removing $Cd^{2+}$ and $Pb^{2+}$ ions. The electron pairs of nitrogen and oxygen atoms in EDTA can form coordination bonds with $Cd^{2+}$ and $Pb^{2+}$ ions. Fig. 17 shows the FT-IR spectra of the adsorbent before and after the adsorption of $Cd^{2+}$ and $Pb^{2+}$ ions. It might be interesting to imagine the environment of the EDTA residues on the surface of the polydopamine. There are carboxylate and carboxylic groups with water molecules hydrogen bonded to these groups. Also, these groups could probably rotate freely. By having this picture in your mind, in the IR spectrum of the EDTA@PD-CNT/$Fe_3O_4$ composite, we observe a strong and broad band in the range of about 1700-1000 $cm^{-1}$, which could be attributed to rotational conformers that lead to splitting or broadening of the carbonyl vibrational bands, stretching of C-O bond that occurs in the range 1320 –1210 $cm^{-1}$ with medium intensity, and the C-O-H bending that appears as a broad and weak band at 1440–1220 $cm^{-1}$, obscured by the $CH_3$ bending. Now, let's look at the IR spectra of the samples coordinated to the $Pd^{2+}$ and $Cd^{2+}$ ions: the broadband seen in the range of about 1700-1000 $cm^{-1}$ has sharpened because of losing free rotation of the carboxylate and carboxylic groups and some of the water molecules, as expected. The peak associated with the vibration frequencies of Pb-O and Cd-O bonds is situated within the 400-700 $cm^{-1}$ range. However, they cannot be observable because of overlapping with the peak related to the vibration frequency of the Fe-O bond. Analysis of the Zeta potential of the ultimate composite verifies the electrostatic attraction between heavy metal and the surface of the adsorbent at the pH under investigation (Scheme 1). The EDS-mapping pictures of the EDTA@PD-CNT/$Fe_3O_4$ adsorbent after the adsorption of $Cd^{2+}$ (Fig. 18(a–g)) and $Pb^{2+}$ (Fig. 18(h–n)) ions provide evidence that adsorption has taken place on the surface and the ions have been uniformly distributed on the surface.

### *3.11. Comparison of adsorbent performance*

Table 6 provides a summary of previous studies involving similar sorbents, which allows comparing their performance. Comparing the performance of the proposed sorbent in this work, i.e., EDTA@PD-CNT/$Fe_3O_4$, with other adsorbents should be interesting from

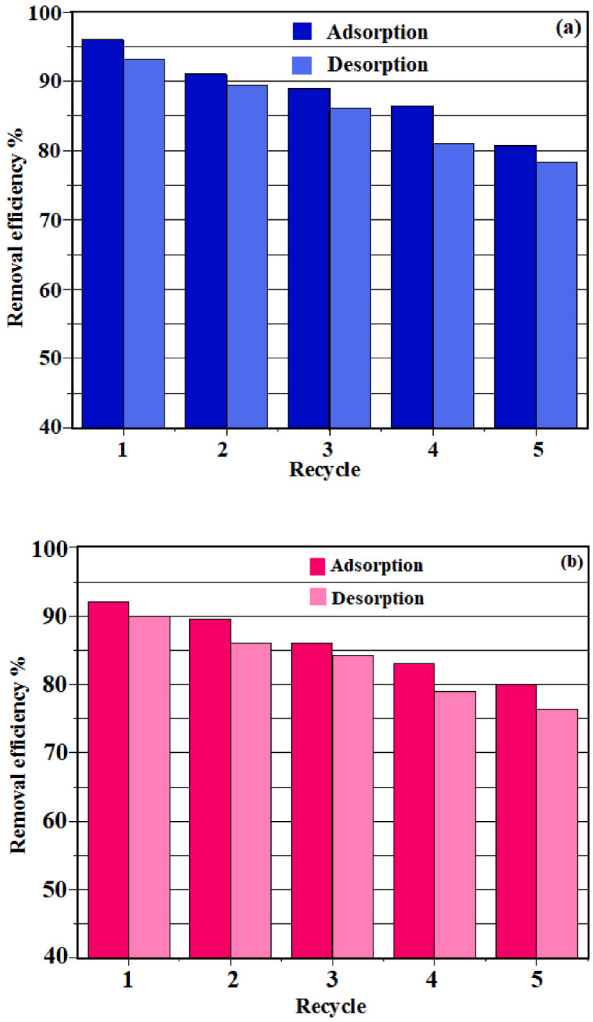


**Fig. 15.** $Pb^{+2}$ (a) and $Cd^{2+}$ (b) removal efficiency from solution by EDTA@PD-CNT/$Fe_3O_4$ during five regeneration.

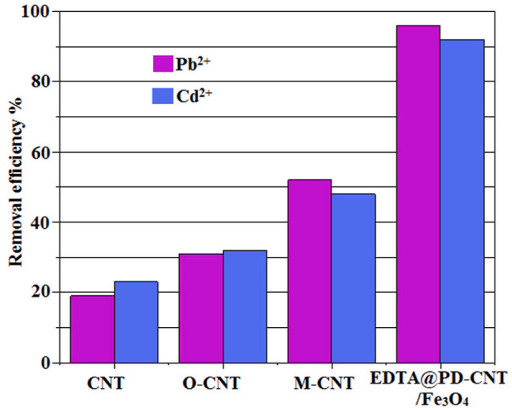


**Fig. 16.** Samples performance evaluations ($C_0$ = 100 mg $L^{-1}$, V = 20 mL, pH = 6, time = 90 min, temperature at 298 K).

this point of view that we relate it to the higher ratio of the EDTA groups anchored to the surface of the polydopamine. For example, the Cell-EDTA adsorbent, which is carboxymethyl cellulose modified with EDTA, has a maximum adsorption capacity of 48.02 mg $g^{-1}$ for cadmium ion and 63.92 mg $g^{-1}$ for lead ion, and the CTP/PAM gel adsorbent modified with EDTA has a maximum adsorption capacity

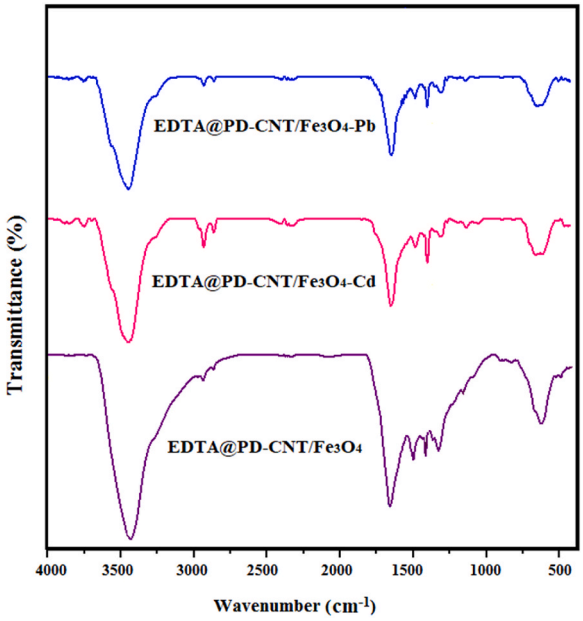


**Fig. 17.** FT-IR spectra of the EDTA@PD-CNT/$Fe_3O_4$ and EDTA@PD-CNT/$Fe_3O_4$ after adsorption of $Cd^{2+}$ and $Pb^{2+}$ ions.

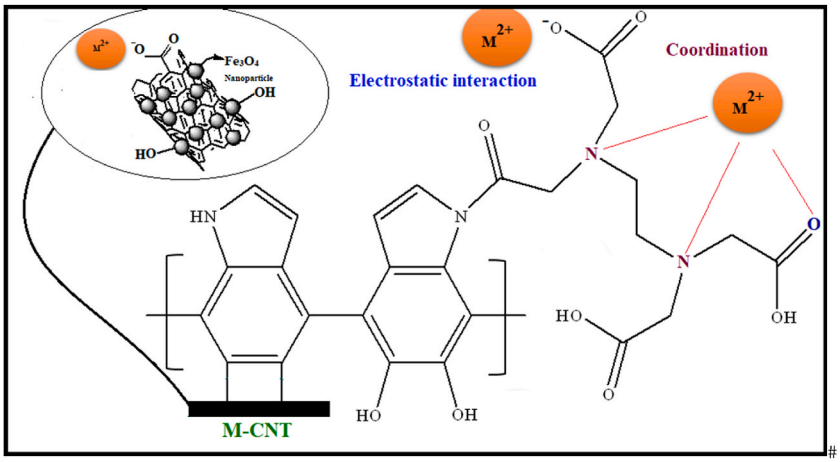


**Scheme 1.** A description of the adsorption mechanism $M^{2+}$($Cd^{2+}$ or $Pb^{2+}$).

of 86.00 mg $g^{-1}$ for cadmium ion and 100.20 mg $g^{-1}$ for lead ion. In this regard, we might be able to claim that the designed adsorbent in this work has advantages, including facile separation, a shorter equilibrium time, a high adsorption capacity, and good recycling after five adsorption cycles. Thus, the synthesized composite has the potential to serve as a very effective adsorbent for wastewater treatment. A study of kinetic and thermodynamics also shows that EDTA@PD-CNT/$Fe_3O_4$ adsorbent, like other adsorbents, follows pseudo-second-order kinetic and the Langmuir isotherm when it comes to adsorbing lead and cadmium ions.

## 4. Conclusion

In the present work, EDTA@PD-CNT/$Fe_3O_4$ adsorbent was made using an easy synthesis method to remove $Pb^{2+}$ and $Cd^{2+}$. A benefit of this adsorbent is its abundance of functional groups on its surface, which can absorb heavy metal ions in water through complex formation with EDTA and electrostatic interaction with oxygen functional groups on the surface of oxidized carbon nanotubes and polydopamine. The magnetic property of the adsorbent accelerates the adsorption process after the treatment and prevents the waste of the adsorbent. The high adsorption capacity for $Pb^{2+}$ and $Cd^{2+}$ was obtained. The adsorption process can be well described by the pseudo-second-order kinetic model, and the Langmuir isotherm is a suitable model for the adsorption process. The synthesized adsorbent was easily recycled and showed 80 % removal efficiency after five adsorption and desorption cycles. Therefore, it can be a

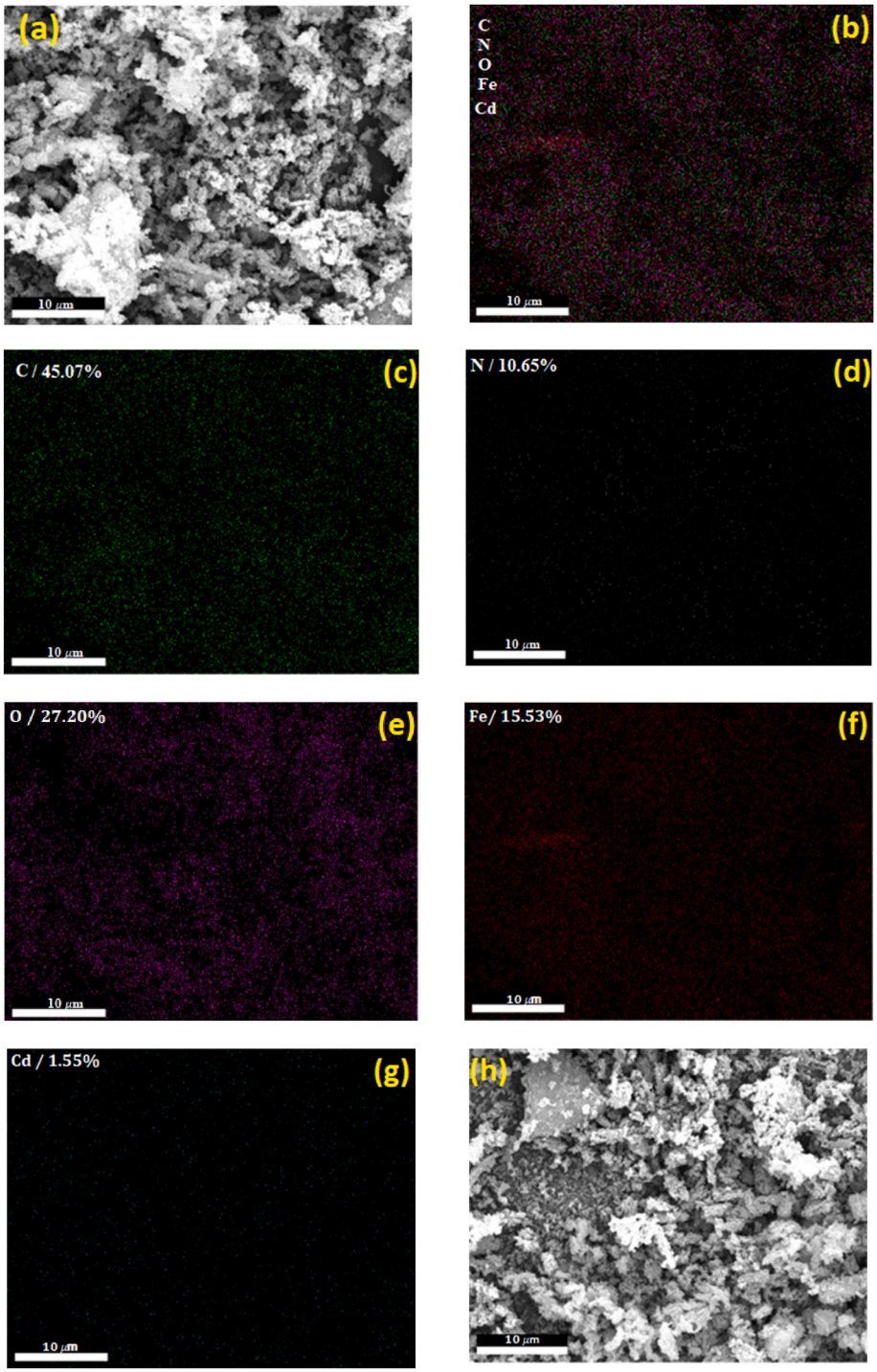


**Fig. 18.** FESEM-EDX mapping images and the corresponding elements of the samples EDTA@PD-CNT/$Fe_3O_4$-Cd (a–g) and EDTA@PD-CNT/$Fe_3O_4$-Pb (h–n).

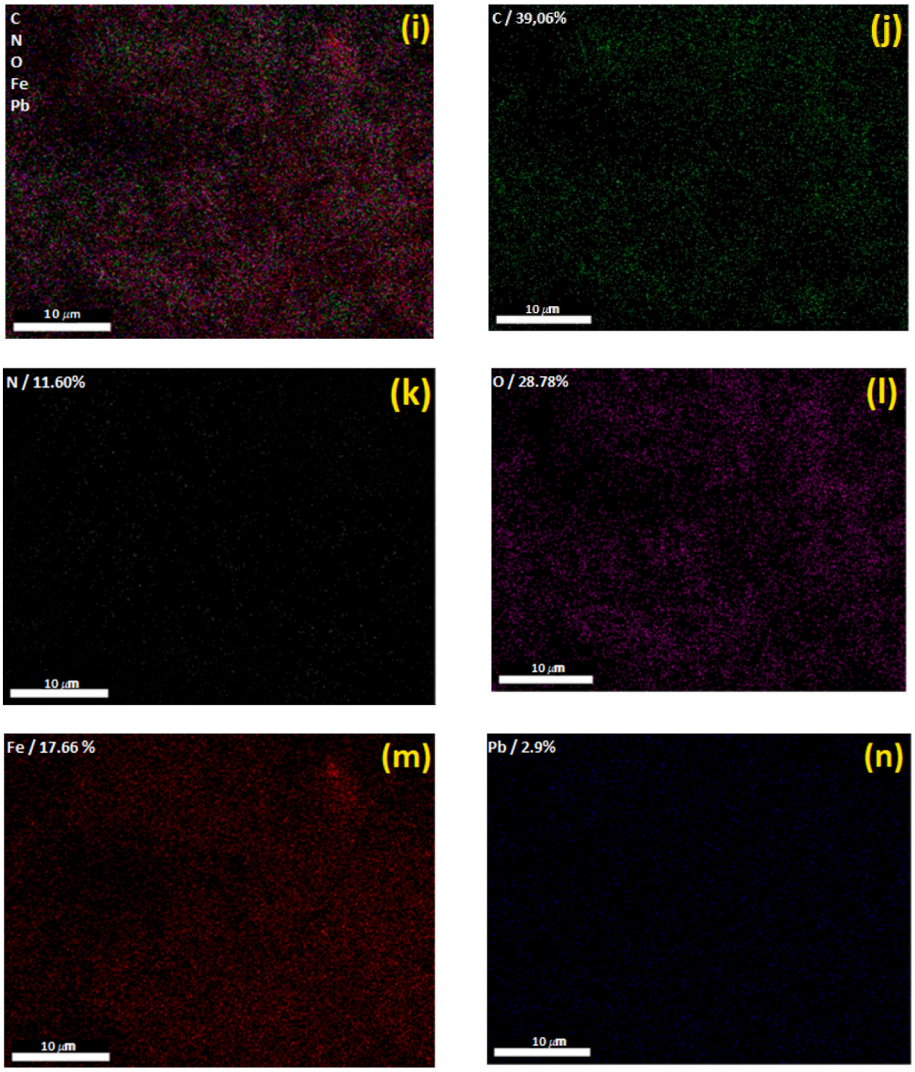


**Fig. 18.** (*continued*).

promising adsorbent with suitable performance in practical works.

## Data availability statement

- Data will be available upon reasonable request from the corresponding authors.

## CRediT authorship contribution statement

**Marzie Esmaeili Chermahini:** Investigation. **Mehran Ghiaci:** Writing – review & editing, Supervision, Conceptualization. **Alireza Najafi Chermahini:** Funding acquisition. **Mehran Shirvani:** Funding acquisition.

## Declaration of competing interest

The authors declare the following financial interests/personal relationships which may be considered as potential competing interests: Ghiaci, Mehran reports financial support was provided by Isfahan University of Technology. If there are other authors, they declare that they have no known competing financial interests or personal relationships that could have appeared to influence the work reported in this paper.

## References


[1] J. Kaur, P. Sengupta, S. Mukhopadhyay, Critical review of bioadsorption on modified cellulose and removal of divalent heavy metals (Cd, Pb, and Cu), Ind. Eng. Chem. Res. 61 (2022) 1921–1954.
[2] Y. Zhang, H. Zheng, P. Zhang, Q. Zuo, B. Zhang, Z. Geng, Y. Yang, X. Ren, A novel post coordination modulation method to synthesize N/S functionalized ZIF-8 for removal of trace heavy metals from drinking water, Appl. Surf. Sci. 615 (2023) 156405.
[3] P. Chen, J. Wu, L. Li, Y. Yang, J. Cao, Modified fly ash as an effect adsorbent for simultaneous removal of heavy metal cations and anions in wastewater, Appl. Surf. Sci. 624 (2023) 157165.
[4] M.K. Abd Elnabi, N.E. Elkaliny, M.M. Elyazied, S.H. Azab, S.A. Elkhalifa, S. Elmasry, M.S. Mouhamed, E.M. Shalamesh, N.A. Alhorieny, A.E. Abd Elaty, Toxicity of heavy metals and recent advances in their removal: a review, Toxics 11 (2023) 580.
[5] R. Gusain, N. Kumar, E. Fosso-Kankeu, S.S. Ray, Efficient removal of Pb (II) and Cd (II) from industrial mine water by a hierarchical MoS2/SH-MWCNT nanocomposite, ACS Omega 4 (2019) 13922–13935.
[6] S. Satarug, Dietary cadmium intake and its effects on kidneys, Toxics 6 (2018) 15.
[7] M.S. Collin, S.K. Venkatraman, N. Vijayakumar, V. Kanimozhi, S.M. Arbaaz, R.S. Stacey, J. Anusha, R. Choudhary, V. Lvov, G.I. Tovar, Bioaccumulation of lead (Pb) and its effects on human: a review, Journal of Hazardous Materials Advances 7 (2022) 100094.
[8] G. Yin, X. Song, L. Tao, B. Sarkar, A.K. Sarmah, W. Zhang, Q. Lin, R. Xiao, Q. Liu, H. Wang, Novel Fe-Mn binary oxide-biochar as an adsorbent for removing Cd (II) from aqueous solutions, Chem. Eng. J. 389 (2020) 124465.
[9] H. Sun, J. Zhan, L. Chen, Y. Zhao, Preparation of CTS/PAMAM/SA/Ca2+ hydrogel and its adsorption performance for heavy metal ions, Appl. Surf. Sci. 607 (2023) 155135.
[10] J. Kulesza, M. Guzinski, M. Bochenska, V. Hubscher-Bruder, F. Arnaud-Neu, Lower rim substituted p-tert-butyl-calix [4] arene. Part 17. Synthesis, extractive and ionophoric properties of p-tert-butylcalix [4] arene appended with hydroxamic acid moieties, Polyhedron 77 (2014) 89–95.
[11] A. Pohl, Removal of heavy metal ions from water and wastewaters by sulfur-containing precipitation agents, Water, Air, Soil Pollut. 231 (2020) 503.
[12] J. Du, B. Zhang, J. Li, B. Lai, Decontamination of heavy metal complexes by advanced oxidation processes: a review, Chin. Chem. Lett. 31 (2020) 2575–2582.
[13] A. Azimi, A. Azari, M. Rezakazemi, M. Ansarpour, Removal of heavy metals from industrial wastewaters: a review, ChemBioEng Rev. 4 (2017) 37–59.
[14] S. Singh, A. Pankaj, S. Mishra, K. Tewari, S.P. Singh, Cerium oxide-catalyzed chemical vapor deposition grown carbon nanofibers for electrochemical detection of Pb (II) and Cu (II), J. Environ. Chem. Eng. 7 (2019) 103250.
[15] I. Trus, M. Gomelya, I. Makarenko, A. Khomenko, G. Trokhymenko, The study of the particular aspects of water purification from the heavy metal ions using the method of nanofiltration, Natsional'nyi Hirnychyi Universytet, Naukovyi Visnyk (2020) 117–123.
[16] S. Bao, W. Yang, Y. Wang, Y. Yu, Y. Sun, One-pot synthesis of magnetic graphene oxide composites as an efficient and recoverable adsorbent for Cd (II) and Pb (II) removal from aqueous solution, J. Hazard Mater. 381 (2020) 120914.
[17] Z. Xie, S. Diao, R. Xu, G. Wei, J. Wen, G. Hu, T. Tang, L. Jiang, X. Li, M. Li, Construction of carboxylated-GO and MOFs composites for efficient removal of heavy metal ions, Appl. Surf. Sci. (2023) 157827.
[18] L. Man, Q. Xu, W. Li, W. Chen, W. Zheng, D.-K. Ma, Oxygen vacancy engineering of Bi2O2CO3 hierarchical microspheres for enhanced adsorption of Cd2+ ions and photocatalytic degradation of Rodamine B, Appl. Surf. Sci. 512 (2020) 145647.
[19] S. Jadoun, J.P. Fuentes, B.F. Urbano, J. Yáñez, A review on adsorption of heavy metals from wastewater using conducting polymer-based materials, J. Environ. Chem. Eng. 11 (2023) 109226.
[20] H.-S. Park, S.-H. Kwak, D. Mahardika, N. Mameda, K.-H. Choo, Mixed metal oxide coated polymer beads for enhanced phosphorus removal from membrane bioreactor effluents, Chem. Eng. J. 319 (2017) 240–247.
[21] S.F. Soares, T. Fernandes, T. Trindade, A.L. Daniel-da-Silva, Recent advances on magnetic biosorbents and their applications for water treatment, Environ. Chem. Lett. 18 (2020) 151–164.
[22] G. Darracq, J. Baron, M. Joyeux, Kinetic and isotherm studies on perchlorate sorption by ion-exchange resins in drinking water treatment, J. Water Proc. Eng. 3 (2014) 123–131.
[23] G.S. Simate, N. Maledi, A. Ochieng, S. Ndlovu, J. Zhang, L.F. Walubita, Coal-based adsorbents for water and wastewater treatment, J. Environ. Chem. Eng. 4 (2016) 2291–2312.
[24] H.S. Abbo, K.C. Gupta, N.G. Khaligh, S.J. Titinchi, Carbon nanomaterials for wastewater treatment, ChemBioEng Rev. 8 (2021) 463–489.
[25] A.E. Burakov, E.V. Galunin, I.V. Burakova, A.E. Kucherova, S. Agarwal, A.G. Tkachev, V.K. Gupta, Adsorption of heavy metals on conventional and nanostructured materials for wastewater treatment purposes: a review, Ecotoxicol. Environ. Saf. 148 (2018) 702–712.
[26] Y. Liu, L. Guo, H. Huang, J. Dou, Q. Huang, D. Gan, J. Chen, Y. Li, X. Zhang, Y. Wei, Facile preparation of magnetic composites based on carbon nanotubes: utilization for removal of environmental pollutants, J. Colloid Interface Sci. 545 (2019) 8–15.
[27] P. Bharadwaj, G.R. Kiran, S.G. Acharyya, Remarkable performance of GO/ZnO nanocomposites under optimized parameters for remediation of Cd (II) from water, Appl. Surf. Sci. 626 (2023) 157238.
[28] Y. Jiang, C. Liu, A. Huang, EDTA-functionalized covalent organic framework for the removal of heavy-metal ions, ACS Appl. Mater. Interfaces 11 (2019) 32186–32191.
[29] J. Wang, J. Zhan, H. Zhou, X. Yi, Y. Liu, Removal of lead from aqueous solution by synergistic interaction between LiCoO2 and tourmaline: synthesis, characterization and mechanism investigation, Appl. Surf. Sci. 631 (2023) 157485.
[30] D. Yuan, W. Liu, J. Wang, J. Cui, L. He, C. Yan, Y. Kou, J. Li, Facile preparation of EDTA-functionalized magnetic chitosan for removal of co (II) from aqueous solutions, Environ. Technol. 42 (2021) 1313–1325.
[31] Y. Huang, A.A. Keller, EDTA functionalized magnetic nanoparticle sorbents for cadmium and lead contaminated water treatment, Water Res. 80 (2015) 159–168.
[32] S. Chen, F. Xie, Selective adsorption of Copper (II) ions in mixed solution by Fe3O4-MnO2-EDTA magnetic nanoparticles, Appl. Surf. Sci. 507 (2020) 145090.
[33] F. Ahmadijokani, S. Tajahmadi, A. Bahi, H. Molavi, M. Rezakazemi, F. Ko, T.M. Aminabhavi, M. Arjmand, Ethylenediamine-functionalized Zr-based MOF for efficient removal of heavy metal ions from water, Chemosphere 264 (2021) 128466.
[34] B. Chen, H. Zhao, S. Chen, F. Long, B. Huang, B. Yang, X. Pan, A magnetically recyclable chitosan composite adsorbent functionalized with EDTA for simultaneous capture of anionic dye and heavy metals in complex wastewater, Chem. Eng. J. 356 (2019) 69–80.
[35] L. Cui, Y. Wang, L. Gao, L. Hu, L. Yan, Q. Wei, B. Du, EDTA functionalized magnetic graphene oxide for removal of Pb (II), Hg (II) and Cu (II) in water treatment: adsorption mechanism and separation property, Chem. Eng. J. 281 (2015) 1–10.
[36] J. Ma, G. Zhou, L. Chu, Y. Liu, C. Liu, S. Luo, Y. Wei, Efficient removal of heavy metal ions with an EDTA functionalized chitosan/polyacrylamide double network hydrogel, ACS Sustain. Chem. Eng. 5 (2017) 843–851.
[37] T. Gong, Y. Tang, Preparation of multifunctional nanocomposites Fe3O4@ SiO2–EDTA and its adsorption of heavy metal ions in water solution, Water Sci. Technol. 81 (2020) 170–177.
[38] A. Daochalermwong, N. Chanka, K. Songsrirote, P. Dittanet, C. Niamnuy, A. Seubsai, Removal of heavy metal ions using modified celluloses prepared from pineapple leaf fiber, ACS Omega 5 (2020) 5285–5296.
[39] M. Xu, Y. Zhang, Z. Zhang, Y. Shen, M. Zhao, G. Pan, Study on the adsorption of Ca2+, Cd2+ and Pb2+ by magnetic Fe3O4 yeast treated with EDTA dianhydride, Chem. Eng. J. 168 (2011) 737–745.
[40] K. Zhang, Z. Dai, W. Zhang, Q. Gao, Y. Dai, F. Xia, X. Zhang, EDTA-based adsorbents for the removal of metal ions in wastewater, Coord. Chem. Rev. 434 (2021) 213809.
[41] R. Zahedi, Z. Asadi, F.D. Firuzabadi, A highly active, recyclable and cost-effective magnetic nanoparticles supported copper catalyst for N-arylation reaction, Catal. Lett. 150 (2020) 65–73.

[42] Y. Xu, L. Gao, Y. Zhou, Synthesis of trifunctional inorganic/organic hybrid nanocomposites and their applications for recognition and elimination of heavy metal ions, Appl. Surf. Sci. 605 (2022) 154659.
[43] V. Silva, P. Andrade, M. Silva, L.D.L.S. Valladares, J.A. Aguiar, Synthesis and characterization of Fe3O4 nanoparticles coated with fucan polysaccharides, J. Magn. Magn Mater. 343 (2013) 138–143.
[44] A.A. Ensafi, N. Zandi-Atashbar, B. Rezaei, M. Ghiaci, M.E. Chermahini, P. Moshiri, Non-enzymatic glucose electrochemical sensor based on silver nanoparticle decorated organic functionalized multiwall carbon nanotubes, RSC Adv. 6 (2016) 60926–60932.
[45] S.K. Park, J. Sure, D.S.M. Vishnu, S.J. Jo, W.C. Lee, I.A. Ahmad, H.-K. Kim, Nano-Fe3O4/carbon nanotubes composites by one-pot microwave solvothermal method for supercapacitor applications, Energies 14 (2021) 2908.
[46] C.-Y. Liu, C.-J. Huang, Functionalization of polydopamine via the aza-michael reaction for antimicrobial interfaces, Langmuir 32 (2016) 5019–5028.
[47] J. Zhang, C.-A. Peng, Poly (N-isopropylacrylamide) modified polydopamine as a temperature-responsive surface for cultivation and harvest of mesenchymal stem cells, Biomater. Sci. 5 (2017) 2310–2318.
[48] Y. Han, X. Wu, X. Zhang, Z. Zhou, C. Lu, Dual functional biocomposites based on polydopamine modified cellulose nanocrystal for Fe3+-pollutant detecting and autoblocking, ACS Sustain. Chem. Eng. 4 (2016) 5667–5673.
[49] S. Zhuang, Q. Zhang, J. Wang, Adsorption of Co2+ and Sr2+ from aqueous solution by chitosan grafted with EDTA, J. Mol. Liq. 325 (2021) 115197.
[50] L. Wang, T. Qi, M. Hu, S. Zhang, P. Xu, D. Qi, S. Wu, H. Xiao, Inhibiting mercury re-emission and enhancing magnesia recovery by cobalt-loaded carbon nanotubes in a novel magnesia desulfurization process, Environ. Sci. Technol. 51 (2017) 11346–11353.
[51] W. Wang, L. Zheng, F. Lu, R. Hong, M.Z. Chen, L. Zhuang, Facile synthesis and characterization of magnetochromatic Fe3O4 nanoparticles, AIP Adv. (2017) 7.
[52] M. Ehteramian, I. Ghasemi, H. Azizi, M. Karrabi, Functionalization of multi-walled carbon nanotube and its effect on shape memory behavior of nanocomposite based on thermoplastic polyurethane/polyvinyl chloride/multi-walled carbon nanotube (TPU/PVC/MWCNT), Iran. Polym. J. (Engl. Ed.) 30 (2021) 411–422.
[53] M. Mahmoudian, Y. Khazani, P. Gozali Balkanloo, M. Enayati, Poly (diallyldimethylammonium chloride)-grafted carboxylated-MWCNT as an additive in the polyethersulfone membrane, Polym. Bull. 78 (2021) 4313–4332.
[54] B. De Menezes, F. Ferreira, B. Silva, E. Simonetti, T. Bastos, L. Cividanes, G. Thim, Effects of octadecylamine functionalization of carbon nanotubes on dispersion, polarity, and mechanical properties of CNT/HDPE nanocomposites, J. Mater. Sci. 53 (2018) 14311–14327.
[55] N. Kurnaz Yetim, F. Kurşun Baysak, M.M. Koç, D. Nartop, Characterization of magnetic Fe 3 O 4@ SiO 2 nanoparticles with fluorescent properties for potential multipurpose imaging and theranostic applications, J. Mater. Sci. Mater. Electron. 31 (2020) 18278–18288.
[56] M.-S. Hong, Y. Park, T. Kim, K. Kim, J.-G. Kim, Polydopamine/carbon nanotube nanocomposite coating for corrosion resistance, Journal of Materiomics 6 (2020) 158–166.
[57] K. Saito, T. Xu, H. Ishikita, Correlation between C= O stretching vibrational frequency and p K a shift of carboxylic acids, J. Phys. Chem. B 126 (2022) 4999–5006.
[58] T. Eom, J. Lee, S. Lee, B. Ozlu, S. Kim, D.C. Martin, B.S. Shim, Highly conductive polydopamine coatings by direct electrochemical synthesis on Au, ACS Appl. Polym. Mater. 4 (2022) 5319–5329.
[59] Z. Wang, W. Xu, F. Jie, Z. Zhao, K. Zhou, H. Liu, The selective adsorption performance and mechanism of multiwall magnetic carbon nanotubes for heavy metals in wastewater, Sci. Rep. 11 (2021) 16878.
[60] P. Akbarzadeh, N. Koukabi, Magnetic carbon nanotube as a highly stable support for the heterogenization of InCl3 and its application in the synthesis of isochromeno [4, 3-c] pyrazole-5 (1H)-one derivatives, Appl. Organomet. Chem. 34 (2020) e5746.
[61] S.-M. Bak, K.-H. Kim, C.-W. Lee, K.-B. Kim, Mesoporous nickel/carbon nanotube hybrid material prepared by electroless deposition, J. Mater. Chem. 21 (2011) 1984–1990.
[62] A. Adam, K. Parkhomenko, P. Duenas-Ramirez, C. Nadal, G. Cotin, P.-E. Zorn, P. Choquet, S. Bégin-Colin, D. Mertz, Orienting the pore morphology of core-shell magnetic mesoporous silica with the sol-gel temperature. influence on MRI and magnetic hyperthermia properties, Molecules 26 (2021) 971.
[63] A. Khedri, D. Jafari, M. Esfandyari, Adsorption of nickel (II) ions from synthetic wastewater using activated carbon prepared from Mespilus germanica leaf, Arabian J. Sci. Eng. 47 (2022) 6155–6166.
[64] F. Zarei, A. Marjani, R. Soltani, Novel and green nanocomposite-based adsorbents from functionalised mesoporous KCC-1 and chitosan-oleic acid for adsorption of Pb (II), Eur. Polym. J. 119 (2019) 400–409.
[65] J. Liang, X. Li, Z. Yu, G. Zeng, Y. Luo, L. Jiang, Z. Yang, Y. Qian, H. Wu, Amorphous MnO2 modified biochar derived from aerobically composted swine manure for adsorption of Pb (II) and Cd (II), ACS Sustain. Chem. Eng. 5 (2017) 5049–5058.
[66] Z. Duan, M. Song, T. Li, S. Liu, X. Xu, R. Qin, C. He, Y. Wang, L. Xu, M. Zhang, Characterization and adsorption properties of cross-linked yeast/β-cyclodextrin polymers for Pb (II) and Cd (II) adsorption, RSC Adv. 8 (2018) 31542–31554.
[67] S. Chang, X. Zhang, C. Wang, J. Bai, X. Li, W. Liang, Y. Mao, J. Cai, Y. Li, Y. Jiang, Efficient adsorption of rhodamine B using synthesized Mg–Al hydrotalcite/sodium carboxymethylcellulose/sodium alginate hydrogel spheres: performance and mechanistic analysis, Heliyon 10 (2024) e30345.
[68] H. Norouzi, D. Jafari, M. Esfandyari, Study on a New Adsorbent for Biosorption of Cadmium Ion from Aqueous Solution by Activated Carbon Prepared from Ricinus communis, 2020.
[69] Z. Huang, C. Xiong, L. Ying, W. Wang, S. Wang, J. Ding, J. Lu, Facile synthesis of a MOF-derived magnetic CoAl-LDH@ chitosan composite for Pb (II) and Cr (VI) adsorption, Chem. Eng. J. 449 (2022) 137722.